

Deterministic printing and heterointegration of single quantum dots

Gregory G. Guymon¹, Hao A. Nguyen², David Sharp³, Tommy Nguyen³, Henry Lei⁴, David S. Ginger², Kai-Mei C. Fu^{3,5,6}, Arka Majumdar^{3,5}, Brandi M. Cossairt², and J. Devin MacKenzie^{1,4,7*}

Affiliations

¹Mechanical Engineering Department, University of Washington; Seattle, 98195, USA.

²Department of Chemistry, University of Washington; Seattle, 98195, USA.

³Department of Physics, University of Washington; Seattle, 98195, USA.

⁴Materials Science Department, University of Washington; Seattle, 98195, USA.

⁵Department of Electrical and Computer Engineering, University of Washington; Seattle, 98195, USA.

⁶Physical Sciences Division, Pacific Northwest National Laboratory, Richland, 99352, USA.

⁷Washington Clean Energy Testbeds, University of Washington; Seattle, 98105, USA.

*Corresponding author (Email: jdmacken@uw.edu)

Abstract

Single quantum dots (QDs) are fundamental building blocks for next-generation quantum photonic technologies, such as single-photon sources and absorbers. Their unique optical properties, including size-tunable emission and high quantum yield¹, make them ideal candidates for applications in secure quantum communication^{2,3}, quantum computing^{4,5}, targeted single-cell and molecular tagging^{6,7}, and sensing^{8,9}. Precisely controlling their placement and heterointegration with photonic structures is crucial for advancing scalable quantum device architectures. Scalable and deterministic heterointegration strategies for single QDs have,

however, remained largely out of reach. Here, we present a new electrohydrodynamic (EHD) printing model that exploits nanoscale dielectrophoretics to precisely print single colloidal QDs with accuracies allowing fully-additive nanoscale photonics integration. Using colossal-shelled QDs solubilized in apolar solvents, this method overcomes continuum fluid surface energetics and stochastic imprecision that limited previous colloidal deposition strategies¹⁰, achieving selective extraction and deposition of individual QDs at sub-zeptoliter volumes. Photoluminescence and autocorrelation function ($g^{(2)}$) measurements confirm nanophotonic cavity-QD integration and the first single-photon emission from printed QDs. This additive, zero-waste nanomanufacturing process offers a scalable, sustainable pathway for the precise heterointegration of nanomaterials down to the single particle level, addressing key limitations in conventional nanofabrication techniques. By enabling deterministic placement of single quantum dots, this method provides a powerful, low carbon footprint platform for fabricating complex photonic circuits and quantum light sources with nanoscale precision. Overall, this new physical printing model represents, in our view, a new way of thinking about heterointegrating quantum scale materials and devices, and a breakthrough of resolution limits to generalized additive nanomanufacturing.

Keywords: Electrohydrodynamic printing; Quantum dots; Additive manufacturing; Single-photon emitters; Nanoparticle integration; Nanophotonics; Nanomanufacturing

Main

The wider proliferation of electronic and photonic devices demands innovations that enable precise, scalable, and less wasteful fabrication of nanoscale components. Among techniques that can directly heterointegrate device elements with diverse physical properties and compositions, additive manufacturing through inkjet printing has emerged as a versatile method for depositing picoliter liquid volumes, with applications ranging from graphic printing to advanced

microelectronics^{11,12} and photonics¹³. Electrohydrodynamic (EHD) printing advances traditional inkjet methods by employing electric fields, as opposed to mechanical or thermal stimuli, to manipulate fluid inks. This technique can readily achieve printed feature resolutions well below 10 μm (Fig. 1a)¹⁴⁻²², enable attoliter-scale droplet deposition, and facilitate direct integration of functional materials onto a variety of substrates. Unlike conventional inkjet droplet formation mechanisms, EHD inkjet printing uses electric fields acting on inks to overcome fluid surface tension barriers that limit other methods. This enables nanoscale control over droplet size and placement through a mechanism that requires no moving parts, allowing it to be readily scaled into parallel multi-nozzle printing modules for higher throughput manufacturing^{23,24}.

Recently, by leveraging dielectrophoretic (DEP) forces, EHD printing has been shown to form and eject sub-attoliter liquid droplets carrying solids by polarizing the particles themselves in nonuniform electric fields^{22,25}. This mechanism generates directional forces on the particles, driving solid-laden fluid along electric field gradients to allow the formation and acceleration of high surface energy small droplets towards a target substrate. Conventionally, the ink fluid has largely been considered as a continuum of liquid and solid constituents, relying on the reduction of printhead nozzle diameters to reduce droplet volumes and nanoparticle counts¹⁷. Here, we demonstrate a new regime of EHD printing, acting on sub-zeptoliter, highly-polarizable, single particles dispersed in relatively non-polarizable solvents, to selectively extract and precisely print individual quantum dots (QDs)—a critical milestone for scalable integration of nanoscale materials. These semiconductor nanocrystals, known for their size-dependent properties, are desirable for next-generation technologies, including optical quantum devices^{26,27}, nanotransistors^{28,29}, sensors⁹, light-emitting diodes^{30,31}, single-photon sources^{8,10}, and CMOS circuits³².

For this study, we selected ligand-dispersed CdSe QDs with colossal CdS shells (80 monolayers) due to their relatively large size (~70 nm in diameter) and high dielectric constant that result in large static electric dipole moments, good dispersion, and optoelectronic stability^{33,34}. In the new EHD printing regime explored here, we have defined electric field and waveform conditions, modeled the electric field environment enabling single QD printing, and determined a QD size range for a given applied electric field to enable selective deposition of single nanoparticles. Furthermore, we have employed this EHD printing mechanism, along with spatial positioning and optical alignment hardware, to pattern single QDs in arrays and achieved deterministic placement of single QDs on nanophotonic cavities. We have also characterized the optical properties of the printed QDs and demonstrated, for the first time, single-photon emission from deterministically printed QDs in arrays and coupled to an optical cavity. We propose this new printing approach as a versatile and precise method for selectively depositing single nanoparticles, offering a transformative pathway for fabricating advanced classical and quantum electronic and photonic devices with nanometer-scale resolution.

DEP principle and colloidal ink design

Fig. 1b schematically illustrates our EHD printing setup for positioning single QD particles. Printing is initiated by applying a voltage between the electrode-integrated glass capillary printhead and the substrate. This creates an electric field that guides the QDs to the substrate. The top inset for Fig. 1b shows a photoluminescence (PL) microscopy image of a capillary printhead loaded with dilute colossal QD suspension showing the presence of isolated emitters that include dispersed single QDs. By varying the printhead-to-substrate standoff height and applied voltage, the electric field intensity can be maximized at the tip interface. Colloidal particles in an “ink” composed of oleic acid capped CdSe/CdS core/shell QDs suspended in an apolar solution mixture are then driven to the tip interface by the electric field. This particle mobility is achieved by

utilizing a medium with a lower relative permittivity than that of the dispersed particles, which gives rise to a polarization disparity between the two that forces the particles towards regions of high electric field intensity. The QDs used in this work were synthesized via a volumetrically tunable strategy that enables the QD core to maintain its quantum-confined optoelectronic characteristics, while increasing the overall size and dipole moment of the particle in an applied field through the shell design (Fig. 1c). The tunable polarization is crucial for generating the DEP forces needed to overcome the net interfacial energies of a single particle, especially when factors like electric field intensity and material properties have finite limits, as discussed in the following sections. The colossal core/shell synthesis yields slightly asymmetric, hexagonal, faceted particles that we approximate as spherical for later numerical and analytical estimations, due to their relatively isotropic morphology³⁵. Our simulation shows that the particle asymmetry is not significantly changing the printing behavior here (Supplementary Fig. 1).

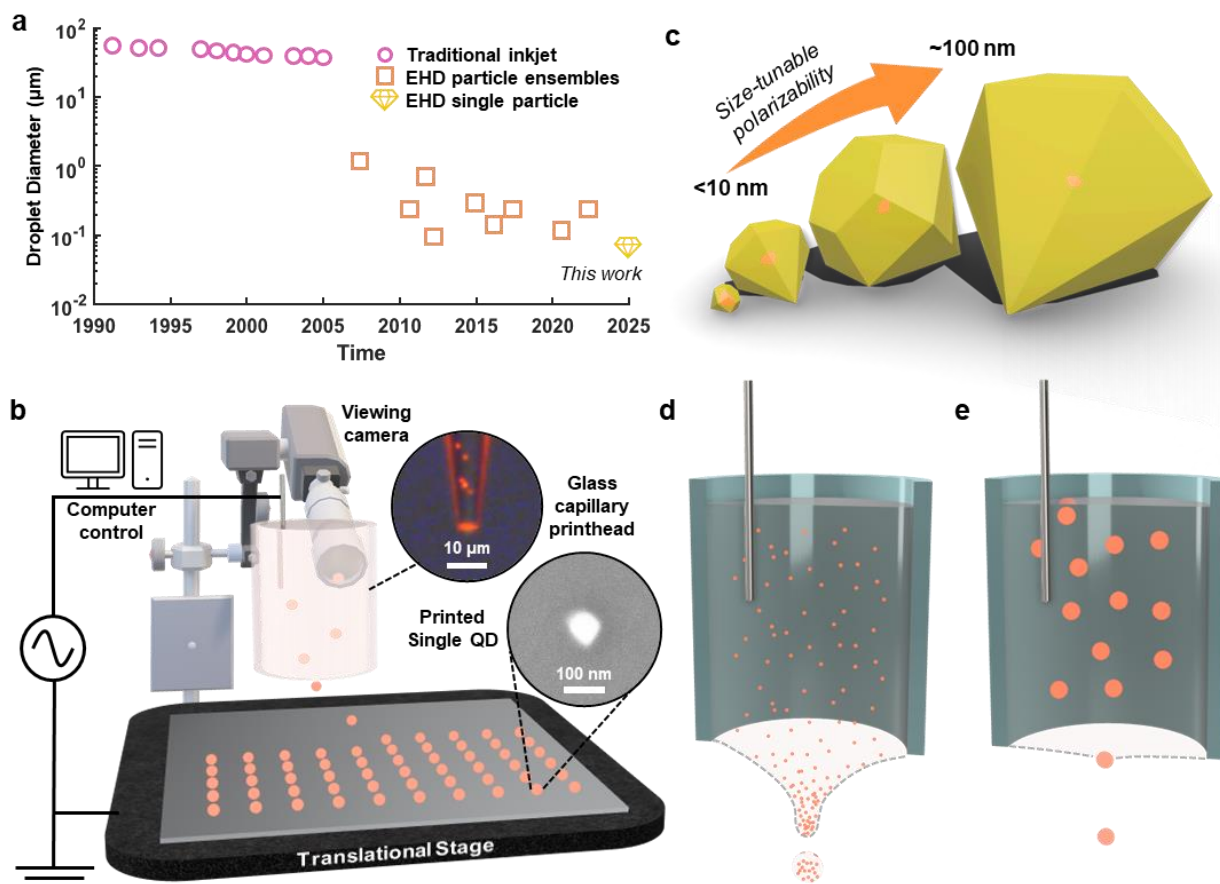


Figure 1: Overview of experiment. **a**, Reported droplet sizes using conventional mechanical inkjet and EHD printing over the past 35 years, along with the results of this work. **b**, Schematic diagram of the EHD printing setup used here. Top inset: fluorescence (FL) microscopy of EHD printhead. Bottom inset: Scanning electron microscopy (SEM) of single EHD-printed QD. **c**, Graphic representation of CdSe QD cores (orange) with tunable range of hexagonal diamond CdS shell (yellow) diameters. **d** and **e**, Bisected illustrations of EHD printheads dielectrophoretically overcoming (d) surface tension to print droplets of particle ensembles and (e) interfacial forces to print singular particles.

Interfacial energy analysis

In order to determine the optimal EHD printing and material design parameters, we first approach the process of separating an individual nanoparticle from a liquid-solid interface by first principles. Each interface in a three-phase system has an associated energy that quantifies the intermolecular interactions dictating the work to expand said interface. These energies can be described as the surface free energy (σ_{SG}), surface tension (σ_{LG}), and interfacial tension (σ_{LS}),

which correspond to the solid-gas, liquid-gas, and liquid-solid interfaces, respectively. By considering the contact angle (θ_{CA}) at the liquid-gas interface, the values can be related to one another via Young's equation:

$$\sigma_{LS} = \sigma_{SG} - \sigma_{LG} \cos(\theta_{CA}) \quad (1)$$

Conventional EHD printing strategies focus on overcoming the energy of surface tension (Fig. 1d) to generate higher area, reversed curvature liquid-gas interfaces in the form of convex Taylor cones and droplets. Alternatively, to separate a particle from a liquid-solid interface, our focus is on overcoming interfacial tension (Fig. 1e). This energy determines the work (W) needed to deform the liquid interface around a particle, where ΔA represents the change in interfacial area as the particle passes through the meniscus interface:

$$W = \sigma \Delta A \quad (2)$$

The total energy required can be determined by considering the net positive and negative changes in the interfacial area for each interface. For a spherical model, the force (F_{net}) required to overcome the net interfacial forces can then be derived with respect to the translational z -axis, i.e. the printing direction towards the target substrate, where a is particle radius:

$$\frac{dW}{dz} = F_{net} = (\sigma_{SG} - \sigma_{LS} - \sigma_{LG})2\pi a \quad (3)$$

We measured the components of interfacial tension (Eq. 1) through optical tensiometry to determine the F_{net} as a function of particle perimeter (see methods). First, we performed a pendant drop test (Supplementary Fig. 2) to determine the surface tension of the apolar solution, which agrees with previously measured values of the solution's constituents³⁶. For the free surface energy of the QDs, we performed a sessile drop test on prepared QD thin films (Fig. 2a), which also agrees with former analysis of the QD ligand chemistry³⁷. We then solved for the interfacial energy in

Eq. 1, resulting in a value of 6.9 ± 1.0 mN/m, which allows us to estimate the F_{net} a single particle needs to overcome to print.

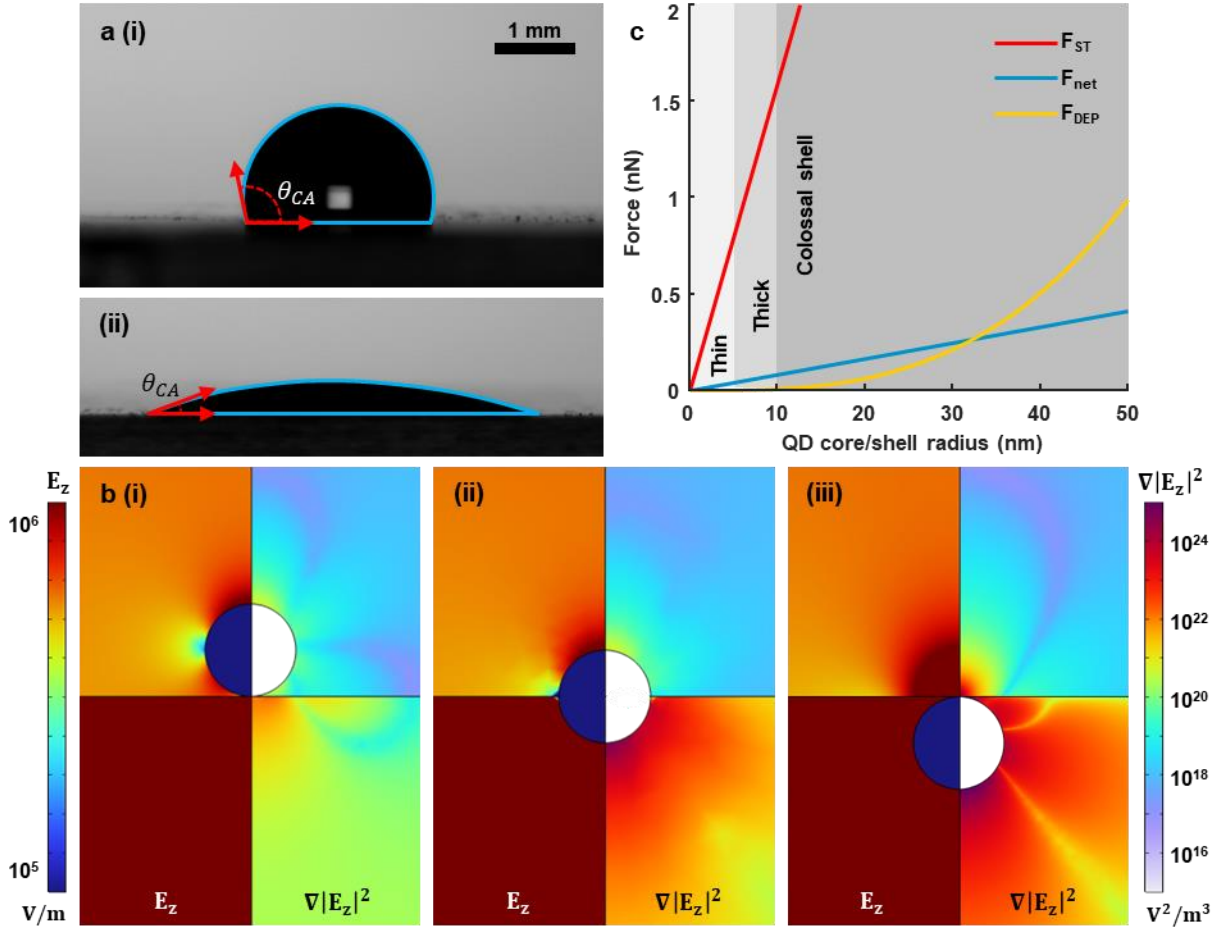


Figure 2: Characterization of ink and energy modeling. **a**, Shadow images of sessile drop shape analysis of (i) water and (ii) octane:hexadecane mixture on CdSe/CdS QD thin film. Sessile droplet outlines (blue) indicate shape profile used for contact angle and surface free energy measurements. **b**, Electrical COMSOL simulation of spherical particle at the (i) interior solution interface, (ii) halfway through solution interface, and the (iii) exterior of the solution interface. The left side of each plot shows the z-component of the electric field (E_z) and the right side shows the z-component of the gradient of the field magnitude squared ($\nabla|E_z|^2$), (the z-axis is normal to the interface). The simulation is symmetrical around the center axis. **c**, Plot of surface tension force (red), net interfacial forces (blue) and DEP forces (yellow) acting on single particles of various radii. The shaded background indicates the size regime of the CdS shells.

Single nanoparticle printing mechanism

The DEP force (F_{DEP}) of a spherical particle under an applied non-uniform AC field can be solved analytically³⁸:

$$F_{DEP} = \pi \varepsilon_m a^3 \Re[k(\omega)] \nabla |E|^2 \quad (4)$$

where ε_m is the real permittivity of the medium and $\nabla |E|^2$ is the gradient of the field magnitude squared for the particle. With the complex permittivities of the particle ($\tilde{\varepsilon}_p$) and medium ($\tilde{\varepsilon}_m$), the direction and magnitude of the force is described by $k(\omega)$, the frequency-dependent Clausius-Mossotti factor:

$$k(\omega) = \frac{\tilde{\varepsilon}_p - \tilde{\varepsilon}_m}{\tilde{\varepsilon}_p + 2\tilde{\varepsilon}_m} \quad (5)$$

Simply put, when the particle is more polarizable than its respective medium, like in the approach we propose here, the particle moves along the electric field gradients towards regions of high field strength, often referred to as positive DEP force, and displaces the less polarizable solvent medium. For QDs with separate core/shell materials, the real component of $\tilde{\varepsilon}_p$ can be calculated as the volumetric ratio between the shell and core's real permittivities³⁹⁻⁴¹. As the shell radius increases past the thin (<5 nm) to the thick (5-10 nm) and into the colossal (10-50 nm) regimes³³, the contribution of the core to $\Re[k(\omega)]$ becomes negligible, asymptotically approaching $\Re[k(\omega)] \approx 0.52$ (Supplementary Fig. 3), assuming a fixed medium permittivity^{42,43}.

We estimate the $\nabla |E|^2$ at the QD particle at the interface of the printhead's fluid meniscus in our EHD printer to be on the order of $\geq 10^{23} \text{ V}^2/\text{m}^3$ using a geometric electrical model by numerically solving Maxwell's equations (COMSOL, Fig. 2b). Using the measured dimensions of the EHD printhead (Supplementary Fig. 4), we simulated the environment around the particle using the maximum voltage bias that our setup can operate at (2 kV). Here, we assume the conductivity of the particle to be similar to CdS thin films, $10^{-7} \sim 10^{-9} \text{ } \Omega^{-1}\text{-cm}^{-1}$, as the CdS constitutes the majority of the material volume at large shell radii⁴⁴⁻⁴⁶. The plotted z-component of the electric field (E_z) shows a high contrast field intensity difference between the solution and

air, which draws the particle towards the higher field intensity. Additionally, the z-component of the gradient of the field magnitude squared plot shows significant field enhancement at the particle, increasing as it passes through the solution interface. Using these estimates, Fig. 2c compares F_{DEP} to F_{net} and pure surface tension force (F_{ST}). Here, we see that F_{DEP} grows exponentially with increasing particle radius, overcoming net interfacial forces as the particle enters the colossal regime. However, the DEP forces at this size are significantly less than what would be expected to form a liquid droplet of equivalent size from solution if we treated the ink solution as a continuum fluid as in conventional models for EHD inkjet. By comparing the competing forces, we estimate that a minimum QD radius ~ 32 nm would be sufficient to overcome the interfacial forces to separate a single QD with our measured interfacial energy from the liquid. To be able to extract and print a single QD and maximize the colloidal stability of these QD solutions, we selected a target particle radius of ~ 35 nm for further experimentation.

It should be noted that the effects of competing forces on the particle's overall force magnitude and direction are minimal. For example, the viscous Stokes drag force (F_{η}) on a particle is equal to the F_{DEP} at terminal velocity in the bulk solution until reaching the interface³⁹. As the particle approaches the meniscus interface, when $F_{DEP} \geq F_{net}$, the particle decelerates, decreasing F_{η} until $F_{DEP} = F_{net} + F_{\eta}$. At this point, the particle continues to move through the interface according to Newton's second law. Consequently, the drag force does not fundamentally impede the particle from crossing the interface. Other forces determined here to be negligible include Brownian motion, gravity, and thermally induced buoyancy.

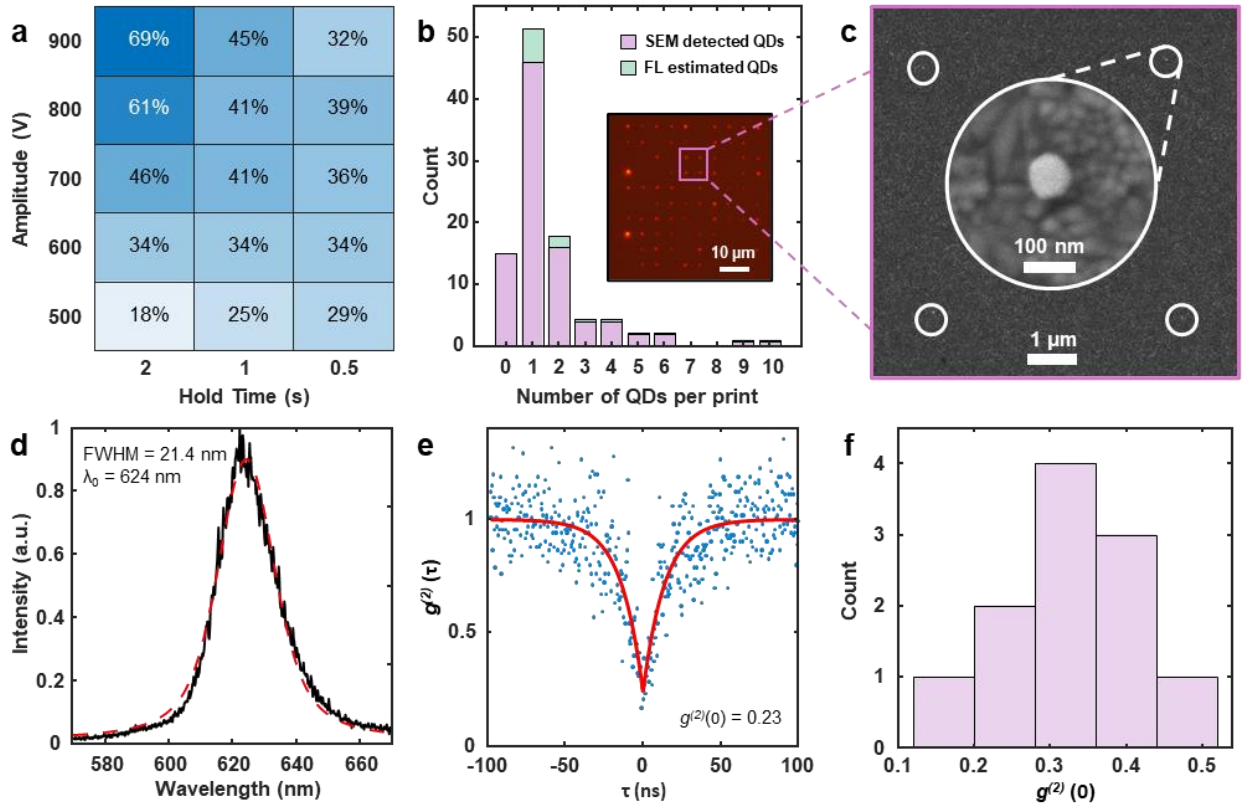


Figure 3: Experimental results of EHD printing colossal QDs. **a**, Effect of drive amplitude on FL detected print yield as a heatmap of number of prints detected out of a 10 x 10 array of print attempt sites, per parameter configuration. **b**, Histogram plot of QDs counted per print site for a 10 x 10 array (900 V and 2 s parameter configuration) of attempt sites, as determined by SEM and FL. Estimated QDs indicate QDs not detected via SEM but were positively-indicated by the FL microscopy (inset). The distribution of estimated QDs is based on the non-zero statistical prevalence QDs per print, per bin. **c**, SEM image of 2 x 2 array of EHD-printed single QDs. White circles indicate single QD positions. Inset: SEM image of single QD. **d**, Plot of single QD emission spectrum (black) and Lorentzian fit (red). **e**, Second-order time correlation plot (blue) and fit (red) of EHD-printed QD showing single-photon emission, measured at room temperature, with 10 μ W excitation (d and e). **f**, Histogram plot of $g^{(2)}(0)$ measurements on EHD-printed single QDs ($n = 11$).

EHD printing single QDs

To test this estimate, we synthesized CdSe/CdS core/shell QDs with a calculated core radius of 1.8 nm and a designed total average radius of 36 ± 3.1 nm from 80 CdS shell monolayers (see methods) and dispersed the particles in octane:hexadecane. Fig. 3a shows the results of an EHD printing trial matrix with this dispersion on ITO-coated SiO₂ across a variety of print electrode

voltage amplitudes (500-900 V) and hold times (0.5-2 s), with a fixed bias (1000 V) and frequency (1 kHz). Here, the hold time refers to the period that the amplitude voltage is applied over a position of interest. Afterwards, using machine vision to count the number of detectable prints (Supplementary Fig. 5), the heatmap shows a gradient of successful QD printing, as determined by fluorescent imaging, over this parameter space in 2D square arrays of one hundred attempts per parameter tested, with each attempt in the arrays spaced by 5 microns in both lateral dimensions on the substrate. As the hold time and amplitude voltage increase, the number of prints made relative to attempts increases. We attribute this trend to a longer period of time for the particle to pass through the meniscus and an increasing strength of electric field applied to the particle, respectively. It should be noted that during this printing process, we could not discern visible meniscus perturbations through high-magnification viewing cameras mounted on the print system, indicating negligible effects of the applied electric fields on the apolar solvent.

Examining the highest print yield array (900 V and 2 s) with SEM (Supplementary Fig. 6 and Supplementary Data 1), Fig. 3b summarizes the number of QDs detected per print via SEM and estimated via FL microscopy. These estimations were from print attempt positions that had emission in FL microscopy, but where QDs were not detected during SEM analysis ($n = 9$). Given the small size and sparseness of the printed QDs in the printed array, the presence of QD luminescence in the FL was taken as absolute proof of printed QDs at the site. We distributed the undetected emitters based on the statistical prevalence of each non-zero count of QDs detected by SEM, resulting in an overall single particle yield of $\sim 50\%$. SEM analysis also revealed single particles for positions with no emission ($n = 7$), indicating that Fig. 3a slightly underestimates the total yields of prints made. We attribute this lack of emission to either non-radiative recombination from excessive defects in the particles, photobleaching by excitation⁴⁷, or QD-excluded CdS

aggregates. Fig. 3c shows a 2 x 2 subarray of single QDs from the larger array. The SEMs show the expected faceted structure consistent with the known morphology of these colossal QDs³³. We call attention to the grain detail of the ITO substrate in the electron micrographs, as well as the lack of any observable drying rings or residue in the vicinity of the particles. Such features are typically observed when a liquid droplet is printed to and wets a substrate⁴⁸. Taken together, the lack of wetting features, in combination with (i) the high surface tension barrier for liquid droplet formation (Fig. 2e, red curve), (ii) the calculated dominance of the dielectric forces for QD over the QD interfacial forces at the meniscus (Fig. 2e, yellow and blue curves), and (iii) negligible interaction of the printing electric fields with the solvents themselves, as expected by the low dielectric constant of the solvent and verified by direct observation of the printing nozzle meniscus, lays out a new model for EHD printing at the nanoscale. Here, we propose the extraction and directed printing of dry or nearly dry core/shell QDs with nanoscale precision from apolar solutions with appropriate surface energies, dielectric properties, and electric field environments for the QDs at the meniscus. We performed experiments with thin-shelled²⁵ and smaller colossal-shelled (Supplementary Fig. 7) CdSe/CdS QDs, and failed to achieve individual particle printing under similar parameters of the EHD setup, again consistent with the proposed model.

Importantly, we also printed single QDs were on insulating silicon nitride substrates with similar parameters to improve the signal-to-noise for spectral analysis. Fig. 3d shows the room temperature photoluminescence spectrum of a single printed QD with an emission peak at 624 nm, and a full-width half-maximum (FWHM) of ~21 nm, consistent with behavior of particles of this composition deposited by conventional drop-casting approaches³³ and measured in solution (Supplementary Fig. 8). Second-order correlation ($g^{(2)}$) measurements on the QDs confirm single-photon emission from printed QDs for the first time. Fig. 3d shows an example of a QD

maintaining its single-photon emissivity ($g^{(2)}(0) < 0.5$) after EHD printing, a critical performance metric for utilizing these materials as single photon sources in quantum computing or networking technologies. Measuring a sample of the EHD-printed single QDs (Fig. 3f) shows a distribution of single-photon emitters, with a mean of $g^{(2)}(0) = 0.33 \pm 0.1$.

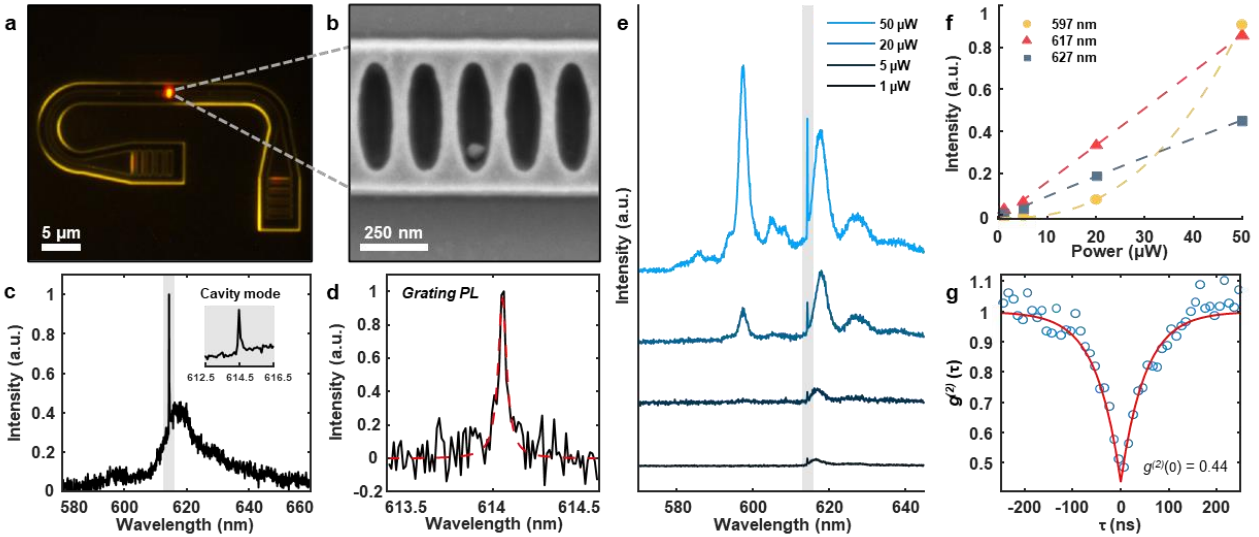


Figure 4: Single QD nanophotonic cavity heterointegration. **a**, Fluorescent microscopy of horseshoe-shaped cavity with single EHD-printed QD. **b**, SEM image of the cavity region containing single QD. **c**, Spectrum plot of cavity integrated QD, at 70 K, excited and measured from the top. Inset: Magnified spectrum (shaded) around the cavity mode. **d**, Spectrum of the pure QD-coupled cavity mode PL to the grating (black) and Lorentzian fit (red) when exciting from the top, measured at room temperature with $10 \mu\text{W}$ excitation (C and D). **e**, Power-dependent spectra of QD-coupled cavity at 8 K with the cavity mode region shaded (614 nm), excited and measured from the top. **f**, Power dependence of 597 nm (yellow), 617 nm (red), and 627 nm (blue) peak intensities at 8 K, with power-law fits (dashed lines). **g**, Second-order time correlation plot (blue) and fit (red) of cavity-coupled QD, excited ($10 \mu\text{W}$) and measured from the top at room temperature.

Nanophotonic cavity heterointegration

To demonstrate the utility of high-resolution single QD printing, we designed a horseshoe-shaped nanophotonic crystal cavity with a resonant frequency of ~ 614.5 nm. We fabricated the cavity with a monolithic waveguide structure that directs emission to rectangular gratings at each end of the horseshoe. Applying the printing strategy described above, we printed a single QD in

the center of the cavity. Fig. 4a shows a FL microscopy image of the emission from the single QD coupling to the waveguide and scattering from the gratings. SEM inspection of the print site (Fig. 4b) confirms the presence of the single QD by identifying the characteristic hexagonal diamond-shaped colossal QD in one of the cavities' central elliptical wells. We note that while the QD is not at the highest intensity point in the cavity, we still expect to observe significant coupling between the QD and the cavity.

The photoluminescence spectrum from the cavity-integrated QD in Fig. 4c reveals the coupling between the cavity's sharp resonant mode and a broad QD emission at 70 K, a condition chosen for its high emission intensity (Supplementary Fig. 9). Examining the narrow spectrum around the cavity mode (Fig. 4c, inset) is consistent with a modest Fano interference, indicated by the characteristic Fano line shape⁴⁹, which is more apparent at room temperature (Supplementary Fig. 10). Measuring the room temperature photoluminescence from the cavity grating, at either end of the horseshoe, isolates emission coupled to the cavity mode. Fig. 4d shows this sharp Lorentzian mode, with a quality factor of 12,500, measured from the Lorentzian fit linewidth over the center wavelength. Similar to our printed QD arrays, photobleaching also occurred in other single QD-integrated cavities, resulting in only the emission from the SiN background and cavity mode (Supplementary Fig. 11).

We measured the QD-cavity system at 8 K across multiple excitation powers (1-50 μW) to examine the broadened tail emission. Fig. 4e shows the separation of the broader emission into an excitonic peak (617 nm) and its phonon sideband (627 nm). At higher power ($>5 \mu\text{W}$), we identify the emergence of a secondary high-energy peak (597 nm), which we attribute to a multi-excitonic transition, accompanied by its own phonon sideband (605 nm). The observed single excitonic and phonon sideband emission is consistent with non-cavity QDs (Supplementary Fig. 12) and the

literature⁵⁰, at low temperature. As shown in Fig. 4f, the exciton and phonon sideband scale nearly linearly with excitation power. The high-energy peak is highly non-linear, with an exponent of 2.5, suggesting a multi-excitonic origin. Lastly, a $g^{(2)}(\tau)$ measurement of the QD-cavity at room temperature (Fig. 4f) shows the coupled system maintaining its single-photon emission.

Conclusion

Colloidal QDs have been discussed for quantum optoelectronic applications since their inception yet have largely been outside of practical considerations due to the challenges associated with their integration into devices. Here, we have demonstrated the first additive nanomanufacturing strategy for deterministically positioning single QDs that exhibit single-photon emission. Not only does this approach allow high throughput printing of large arrays of dots at room temperature, without resorting to vacuum processing or lithography, but it also allows for the positioned deposition of dots into prefabricated nanophotonic elements such as high-Q cavities. We propose that this printing is enabled by a new mechanism for electrohydrodynamic printing: dielectrophoretic expulsion of essentially dry, highly polarizable single particles from a relatively non-interacting solvent medium. This mechanism requires particles with sufficient dielectric contrast from the solvent, which can be realized with typical semiconductor nanocrystals at sizes that are now synthetically achievable. While we used colossal (~70 nm) CdSe/CdS particles here, we estimate the method should be applicable to a range of other colloidal nanoparticles, from halide perovskites, to nanodiamonds, opening the door to a scalable, contactless, zero-wasted additive nanomanufacturing process that can be conducted at ambient conditions to enable the positioning of single discrete colloidal QDs. These results represent significant progress in realizing scalable photonic qubit platforms and the future development of quantum optoelectronics. We also believe this represents a step forward for the additive

manufacturing of materials, where low-waste printing processes can match and even exceed the capabilities of conventional subtractive and complex semiconductor fabrication processes.

References

1. Efros, A. L. & Brus, L. E. Nanocrystal Quantum Dots: From Discovery to Modern Development. *ACS Nano* **15**, 6192–6210 (2021).
2. Wang, J., Sciarrino, F., Laing, A. & Thompson, M. G. Integrated photonic quantum technologies. *Nat. Photonics* **14**, 273–284 (2020).
3. Paraiso, T. K. *et al.* A photonic integrated quantum secure communication system. *Nat. Photon.* **15**, 850–856 (2021).
4. Slussarenko, S. & Pryde, G. J. Photonic quantum information processing: A concise review. *Applied Physics Reviews* **6**, 041303 (2019).
5. Elshaari, A. W., Pernice, W., Srinivasan, K., Benson, O. & Zwiller, V. Hybrid integrated quantum photonic circuits. *Nat. Photonics* **14**, 285–298 (2020).
6. Zrazhevskiy, P. & Gao, X. Quantum dot imaging platform for single-cell molecular profiling. *Nat. Commun.* **4**, 1619 (2013).
7. Ma, Y. *et al.* Live cell imaging of single genomic loci with quantum dot-labeled TALEs. *Nat. Commun.* **8**, 15318 (2017).
8. Kagan, C. R., Bassett, L. C., Murray, C. B. & Thompson, S. M. Colloidal Quantum Dots as Platforms for Quantum Information Science. *Chem. Rev.* **121**, 3186–3233 (2021).
9. Chang, J., Gao, J., Zadeh, I. E., Elshaari, A. W. & Zwiller, V. Nanowire-based integrated photonics for quantum information and quantum sensing. *Nanophotonics* **12**, 339–358 (2023).
10. Nguyen, H. A. *et al.* Design Rules for Obtaining Narrow Luminescence from Semiconductors Made in Solution. *Chem. Rev.* **123**, 7890–7952 (2023).

11. Tilford, T. *et al.* Comparative Reliability of Inkjet-Printed Electronics Packaging. *IEEE Trans. Compon. Packag. Manuf. Technol.* **11**, 351–362 (2021).
12. Liu, Y. *et al.* Inkjet Printed Metal–Organic Frameworks for Non-Volatile Memory Devices Suitable for Printed RRAM. *Adv. Funct. Mater.* **n/a**, 2412372.
13. Liu, Y. *et al.* Efficient All-Solution Processed Quantum Dot Light Emitting Diodes Based on Inkjet Printing Technique. *ACS Appl. Mater. Interfaces* **9**, 25506–25512 (2017).
14. Fujii, M. Evolution Theory of Ink Jet Technologies: Progress by Component or Architectural Knowledge. *JIST* **62**, 040502-1-040502–7 (2018).
15. Park, J. U. *et al.* High-resolution electrohydrodynamic jet printing. *Nat. Mater.* **6**, 782–789 (2007).
16. Niklas Schirmer, B. C. *et al.* On Ejecting Colloids Against Capillarity from Sub-micrometer Openings: On-Demand Dielectrophoretic Nanoprinting. *Adv. Mater.* **22**, 4701–4705 (2010).
17. Galliker, P. *et al.* Direct printing of nanostructures by electrostatic autofocussing of ink nanodroplets. *Nat. Commun.* **3**, 890 (2012).
18. Kim, B. H. *et al.* High-resolution patterns of quantum dots formed by electrohydrodynamic jet printing for light-emitting diodes. *Nano Lett.* **15**, 969–973 (2015).
19. Richner, P. *et al.* Printable Nanoscopic Metamaterial Absorbers and Images with Diffraction-Limited Resolution. *ACS Appl. Mater. Interfaces* **8**, 11690–11697 (2016).
20. Zhang, B. *et al.* One-Step Sub-micrometer-Scale Electrohydrodynamic Inkjet Three-Dimensional Printing Technique with Spontaneous Nanoscale Joule Heating. *ACS Appl. Mater. Interfaces* **9**, 29965–29972 (2017).
21. Rohner, P. *et al.* 3D electrohydrodynamic printing and characterisation of highly conductive gold nanowalls. *Nanoscale* **12**, 20158–20164 (2020).

22. Cohen, T. A. *et al.* Direct Patterning of Perovskite Nanocrystals on Nanophotonic Cavities with Electrohydrodynamic Inkjet Printing. *Nano Lett.* **22**, 5681–5688 (2022).
23. Lee, J.-S. *et al.* Design and evaluation of a silicon based multi-nozzle for addressable jetting using a controlled flow rate in electrohydrodynamic jet printing. *Appl. Phys. Lett.* **93**, 243114 (2008).
24. Khan, A. *et al.* Fabrication of circuits by multi-nozzle electrohydrodynamic inkjet printing for soft wearable electronics. *JMR* **36**, 3568–3578 (2021).
25. Guymon, G. G. *et al.* Electrohydrodynamic Printing-Based Heterointegration of Quantum Dots on Suspended Nanophotonic Cavities. *Adv. Mater. Technol.* **9**, 2301921 (2024).
26. Choi, J.-H. *et al.* Exploiting the colloidal nanocrystal library to construct electronic devices. *Science* **352**, 205–208 (2016).
27. Olshansky, J. H. *et al.* Using Photoexcited Core/Shell Quantum Dots To Spin Polarize Appended Radical Qubits. *J. Am. Chem. Soc.* **142**, 13590–13597 (2020).
28. Hetsch, F., Zhao, N., Kershaw, S. V. & Rogach, A. L. Quantum dot field effect transistors. *Mater. Today* **16**, 312–325 (2013).
29. Shibata, K. *et al.* Single PbS colloidal quantum dot transistors. *Nat. Commun.* **14**, 7486 (2023).
30. Kovalenko, M. V., Protesescu, L. & Bodnarchuk, M. I. Properties and potential optoelectronic applications of lead halide perovskite nanocrystals. *Science* **358**, 745–750 (2017).
31. Shamsi, J., Rainò, G., Kovalenko, M. V. & Stranks, S. D. To nano or not to nano for bright halide perovskite emitters. *Nat. Nanotechnol.* **16**, 1164–1168 (2021).

32. Yun, H. J. *et al.* Solution-processable integrated CMOS circuits based on colloidal CuInSe₂ quantum dots. *Nat. Commun.* **11**, 5280 (2020).
33. Nguyen, H. A. *et al.* Colossal Core/Shell CdSe/CdS Quantum Dot Emitters. *ACS Nano* **18**, 20726–20739 (2024).
34. Chen, Y. *et al.* “Giant” Multishell CdSe Nanocrystal Quantum Dots with Suppressed Blinking. *J. Am. Chem. Soc.* **130**, 5026–5027 (2008).
35. Cao, W., Chern, M., Dennis, A. M. & Brown, K. A. Measuring Nanoparticle Polarizability Using Fluorescence Microscopy. *Nano Lett.* **19**, 5762–5768 (2019).
36. Klein, T. *et al.* Liquid Viscosity and Surface Tension of n-Hexane, n-Octane, n-Decane, and n-Hexadecane up to 573 K by Surface Light Scattering. *J. Chem. Eng. Data* **64**, 4116–4131 (2019).
37. Kallio, T., Laine, J. & Stenius, P. Intermolecular Interactions and the Adhesion of Oleic Acid. *J. Disper. Sci. Technol.* **30**, 222–230 (2009).
38. Green, N. G. & Nili, H. Dielectrophoresis. in *Encyclopedia of Nanotechnology* (ed. Bhushan, B.) 534–543 (Springer Netherlands, Dordrecht, 2012). doi:10.1007/978-90-481-9751-4_131.
39. Hywel, M. & Green, N. *AC Electrokinetics: Colloids and Nanoparticles*. (Research Studies Press, 2003).
40. Goyal, M. & Singh, M. Size and shape dependence of optical properties of nanostructures. *Appl. Phys. A* **126**, 176 (2020).
41. Suresh, S. & Arunseshan, C. Dielectric Properties of Cadmium Selenide (CdSe) Nanoparticles synthesized by solvothermal method. *Appl. Nanosci.* **4**, 179–184 (2014).
42. Trewby, W. & Voitchovsky, K. Nanoscale probing of local dielectric changes at the interface between solids and aqueous saline solutions. *Faraday Discuss.* **246**, 387–406 (2023).

43. Pirolli, L., Goodwin, A. R. H., Marsh, K. N. & May, E. F. Determination of the Relative Permittivity, ϵ_r , of Octane at Temperatures between (303 and 393) K and Pressures below 25 MPa with a Concentric Cylinder Capacitor at a Frequency of 1 kHz. *J. Chem. Eng. Data* **59**, 1609–1613 (2014).
44. Moualkia, H., Hariech, S., Aida, M. S., Attaf, N. & Laifa, E. L. Growth and physical properties of CdS thin films prepared by chemical bath deposition. *J. Phys. D: Appl. Phys.* **42**, 135404 (2009).
45. Nair, P. K., nair, M. T. S., Campos, J. & Sansores, L. E. A critical discussion of the very high photoconductivity in chemically deposited cadmium sulfide thin films: Implications for solar cell technology. *Solar Cells* **22**, 211–227 (1987).
46. Martínez-Landeros, V. H., Hernandez-Como, N., Gutierrez-Heredia, G., Quevedo-Lopez, M. A. & Aguirre-Tostado, F. S. Structural, chemical and electrical properties of CdS thin films fabricated by pulsed laser deposition using varying background gas pressure. *Thin Solid Films* **682**, 24–28 (2019).
47. Lee, S. F. & Osborne, M. A. Brightening, Blinking, Bluing and Bleaching in the Life of a Quantum Dot: Friend or Foe? *ChemPhysChem* **10**, 2174–2191 (2009).
48. Onses, M. S., Sutanto, E., Ferreira, P. M., Alleyne, A. G. & Rogers, J. A. Mechanisms, Capabilities, and Applications of High-Resolution Electrohydrodynamic Jet Printing. *Small* **11**, 4237–4266 (2015).
49. Limonov, M. F., Rybin, M. V., Poddubny, A. N. & Kivshar, Y. S. Fano resonances in photonics. *Nat. Photon.* **11**, 543–554 (2017).
50. Berkinsky, D. B. *et al.* Narrow Intrinsic Line Widths and Electron–Phonon Coupling of InP Colloidal Quantum Dots. *ACS Nano* **17**, 3598–3609 (2023).

Materials and Methods

Chemicals and Materials

All chemicals listed below were used without further purification, unless stated otherwise. Oleic acid ($\geq 90\%$), anhydrous methyl acetate (99.5%), selenium powder (99.999%, 100 mesh), cadmium oxide powder (CdO, 99.9%), trioctylphosphine oxide (TOPO, 99%), trioctylphosphine (TOP, 90%), 1-octanethiol (99%), 1-octadecene (ODE, 90%), n-octane (98%), hexadecane (99%), and anhydrous hexane (95%) were purchased from MilliporeSigma, and n-octadecylphosphonic acid (ODPA, 99%) was purchased from PCI Synthesis. Cadmium oleate solution (0.2 M in ODE) was made by heating CdO (2.57 g), oleic acid (63 mL), and ODE (27 mL) at 160 °C for 30 min, followed by evacuating the solution at 110 °C for 1 h.

Methods

CdSe QD Synthesis

The synthesis of colossal CdSe/80CdS QDs (CdSe with 80 monolayers (ML) of CdS) was conducted according to methods reported previously³³. The wurtzite CdSe core synthesis started with adding TOPO (3 g), CdO (0.06 g), ODPA (0.28 g), and a magnetic stir bar to a 15 mL three-neck round-bottom flask secured with a septum, a thermowell equipped with a thermometer, and a condenser. The flask was put under vacuum for 30 min at 100 °C, then was refilled with N₂. The temperature was then set to 375 °C. A dropwise addition of TOP (1.5 mL) was done while the temperature was ramping up from 320 to 370 °C. When the temperature was at 375 °C, a pre-prepared solution of Se powder (0.058 g) dissolved in TOP (0.4 mL) was quickly injected. After 45 s, the flask was quickly cooled to room temperature with forced air to yield CdSe QDs. The QDs were purified in a glovebox by centrifugation with methyl acetate/hexane and were stored in hexane.

Shelling of CdSe with CdS

ODE (6 mL) was added into a 25 mL three-neck round-bottom flask secured with a septum, a thermowell equipped with a thermometer, and a condenser, which was put under vacuum at 110 °C for 60 min, then refilled with N₂ gas. An amount of CdSe core in hexane (typically 5–100 nmol) was added to the flask. Hexane was completely removed by evacuating the flask 110 °C for 30. The flask was then heated to 310 °C. When the temperature was at 260 °C, 0.2 M Cd(oleate)₂ and 0.2 M 1-octanethiol solutions were slowly injected into the reaction flask using a dual-syringe pump with the rate of 3 mL/h. The volumes of the shell precursors were calculated to achieve 30 MLs of CdS shells on QD cores with a diameter of ~3.5 nm. After the injection finished, the reaction was annealed at 280 °C for 2 h, then cooled down to 60 °C. Without purification, a portion of the yellow CdSe₃₀CdS solution was transferred to a different 3-neck round-bottom flask for another shelling step that targeted additional 20 CdS MLs to achieve CdSe₅₀CdS using the same shelling procedure. This step was repeated one more time to achieve CdSe₈₀CdS. The final product was purified in a glovebox with hexane and then stored in hexane. Detailed calculations of shell precursor amounts were described in a previous report³³.

QD Ink Preparation

The QD ink was prepared by evaporating a hexane-based QD solution under vacuum at 100 °C for 30 min, yielding ~3 mg of bright yellow QD powder. The resulting powder was subsequently dispersed in 10 mL of a 1:1 octane:hexadecane mixture through stirring at 80 °C for 1 h, followed by sonication 1 h.

Pendant Drop Tensiometry

The video image was calibrated to the outer diameter of the dispensing syringe of a Krüss drop shape analyzer to establish the scale and obtain accurate drop dimensions. The shape of the drop

was then analyzed through grayscale shadow image processing. A shape parameter was adjusted iteratively by a Young-Laplace numerical model until the computed drop shape matched the observed one. Finally, the surface tension was calculated, based on the solution density and the optimized shape parameter, to be 25.3 ± 0.3 mN/m.

Sessile Drop Tensiometry

A substrate for the sessile drop tensiometry was prepared via spin coating CdSe/CdS on a glass substrate. Using a Krüss drop shape analyzer, a drop was deposited onto the solid sample, and its image was captured using a camera, then processed through drop shape analysis software. The drop's contour was first identified using grayscale shadow image analysis. Next, a geometric model was applied to fit the identified contour. The contact angle was determined as the angle between the fitted drop shape and the surface of the sample. These were determined as $92.3^\circ \pm 2.0^\circ$ and $18.5^\circ \pm 2.9^\circ$ for water and 1:1 octane:hexadecane, respectively. After the drop shape and contact angle were measured, the surface free energy of the solid sample was calculated, using a combination of contact angles from multiple probe liquids (water and 1:1 octane:hexadecane) with known surface tensions, to be 30.8 ± 1.0 mN/m.

Finite Element Analysis

Simulation was performed with the electric current (EC) package within the AC/DC Module using COMSOL Multiphysics. Permittivity and conductivity of the materials were used to perform the simulation. Physical dimensions of the components were modeled after micrographs (printing nozzle), SEM characterization (quantum dot) and measured substrate thickness. A source voltage of 2000 V was used as a stimulus to the electrode voltage, and the printing bed was used as the reference ground for the applied voltage, both analogous to the actual printing setup. A 2D axial

rotationally symmetric simulation was performed for the analysis. A flat meniscus was assumed for the liquid-gas interface.

Electrohydrodynamic Inkjet Printing

Electrohydrodynamic inkjet printing was conducted by loading the prepared CdSe/CdS ink into pulled borosilicate glass capillary pipettes with a tip internal nozzle diameter of $\sim 5 \mu\text{m}$. These printheads were manufactured with a tungsten electrode filament integrated inside this pipette. After mounting the printhead into the printer and placing the substrate on a grounded stage vacuum chuck, printing could be initiated. For the nanophotonic cavity, an alignment process was used to map the designed printing pattern to the orientation of the target substrate. Upon completion, printing was initiated with the following parameters: bias: 1000 V, amplitude: 900-1000 V, frequency: 1 kHz, hold time 1-2 seconds.

Photoluminescence Characterization of Bare Substrate QD

Single-particle characterization was performed in air using a custom-built scanning PL set-up. A 532 nm continuous-wave laser (Laserglow Technologies 532 nm DPSS Laser) was focused on the particles with a 100 \times (NA 0.95) dry objective lens with a typical excitation power of 10 μW . The laser spot position was controlled via a steering mirror (Newport FSM-300-01). The collected PL was filtered through both a 550 nm long-pass filter and a bandpass filtered centered on 618 nm with 50 nm bandwidth. The collected PL was fiber-coupled either to a spectrometer (Princeton Instruments Isoplan 100) to collect the single-particle spectrum or through a 50:50 fiber splitter to a pair of avalanche photodiodes (MPD-PDM) to collect the $g^{(2)}$ spectrum. For the $g^{(2)}$ spectra, the time correlation was performed via a time tagger (PicoQuant TimeHarp 260).

Nanophotonic Cavity Fabrication

The SiN nanobeam cavities were designed for operation on a SiO₂ substrate with no top cladding in 220 nm thick SiN. The cavity was formed by punching a one-dimensional array of elliptical holes in a 550 nm wide SiN waveguide. The dimensions of the elliptical holes were fixed to a major diameter of 411 nm and a minor diameter of 98 nm. Each half of the cavity consisted of 10 elliptical holes that quadratically tapered from a period of 184 nm to 190 nm. An additional 20 elliptical holes with a period of 193 nm were placed on either end to form the cavity mirrors. According to FDTD simulations, this resulted in a cavity mode at 618 nm with quality factor $\sim 4 \times 10^5$ and mode volume $\sim 2 (\lambda/n)^3$. To fabricate the nanobeam cavities, 100 kV ebeam-lithography was used to transfer the pattern to a positive-tone ebeam resist. The pattern was then etched into the SiN thin film using a fluorine-based plasma etch.

Photoluminescence Characterization of Cavity-Integrated QD

Measurements were performed in a confocal setup operating in ambient conditions. Green continuous wave 532nm laser light (LaserQuantum opus532) was passed through a 532 dichroic mirror (Chroma ZT532RDC) focused onto the center of the cavity using a 40x/0.6 NA Olympus objective, with a 1 μ m spot size. A 580LP was used to filter out excitation light and PL went to a Princeton Instruments 300 grooves/mm grating spectrometer (SpectraPro HRS-750) coupled to a Pixis CCD (PIXIS: 100BR_eXcelon). Confocal scans were performed using a SPCM (Excelitas SPCM-AQ4C) coupled to a NIDAQ (BNC-2110). g_2 was measured by going through a 40:60 fiber beam splitter and a timetagter (Swabian Instruments Timetagter Ultra). All low temperature measurements were done with a Montana cryostat (cryostation S-series) operating at 8K. Peaks in Fig 4E were integrated and fit to a power law $I = aP^b$ (Fig. 4f), with the emission intensities scaling with excitation power (P) : excitonic (P¹), multi-excitonic (P² or higher), and phonon-assisted (P¹ or higher).

Data and materials availability: All data are available in the main text or the supplementary information.

Acknowledgements: We thank Ethan Schwartz for ITO/glass substrate preparation.

Author contributions:

Conceptualization: GGG, HL, JDM

Methodology: GGG, HAN, HL, JDM

Investigation: GGG, HAN, DS, TN, HL

Visualization: GGG, HAN, TN

Funding acquisition: JDM, BMC, AM, KCF, DSG

Project administration: JDM, BMC, AM, KCF

Supervision: JDM, BMC, AM, KCF

Writing – original draft: GGG, HL, JDM

Writing – review & editing: GGG, HAN, DS, TN, HL, DSG, KCF, AM, BMC, JDM

Competing interests: Authors declare that they have no competing interests.

Funding:

National Science Foundation (NSF) Center for Integration of Modern Optoelectronic Materials on Demand (IMOD), an NSF Science and Technology Center, under grant agreement DMR-2019444 (JDM, BMC, AM, KCF, DSG)

Molecular Analysis Facility, which is supported in part by funds from the Molecular Engineering & Sciences Institute, the Clean Energy Institute, and the National Science Foundation (NNCI-2025489 and NNCI-1542101)

Washington Research Foundation (AM, KCF, JDM)

Joint Center for Deployment and Research in Earth Abundant Materials (JDM)

Washington Clean Energy Testbeds, a facility operated by the University of Washington Clean Energy Institute,

Air Force Research Laboratory with SEMI-FlexTech (JDM, HL) under Agreement Number FA8650-20-2-5506 in support of Army Research Laboratory.

Supplementary Information for

Deterministic printing and heterointegration of single quantum dots

Gregory G. Guymon, Hao A. Nguyen, David Sharp, Tommy Nguyen, Henry Lei, David S. Ginger, Kai-Mei C. Fu, Arka Majumdar, Brandi M. Cossairt, and J. Devin MacKenzie*

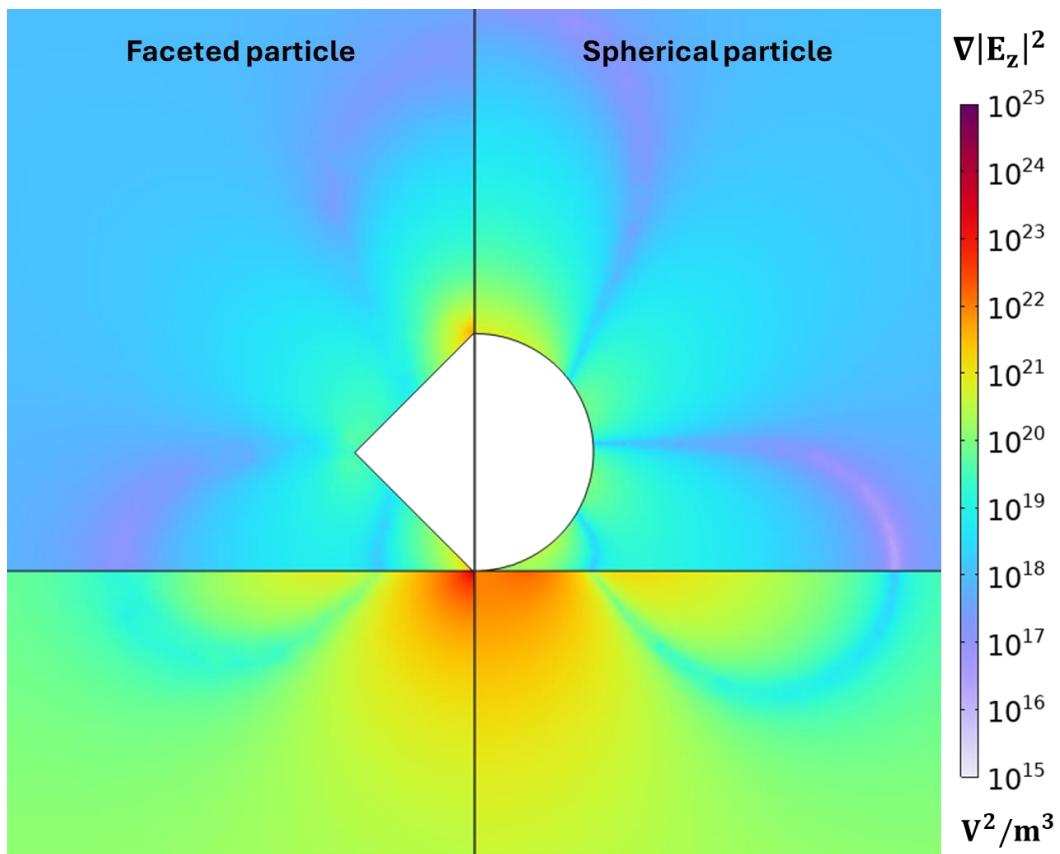
Corresponding author: jdmacken@uw.edu

The PDF file includes:

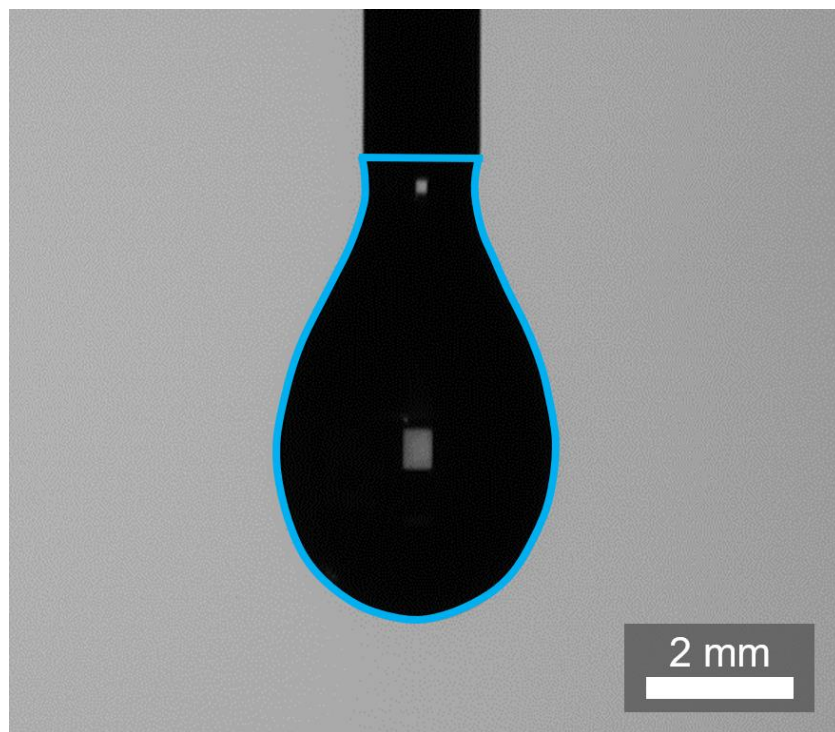
Supplementary Figs. 1 to 12

Other Supplementary Information for this manuscript include the following:

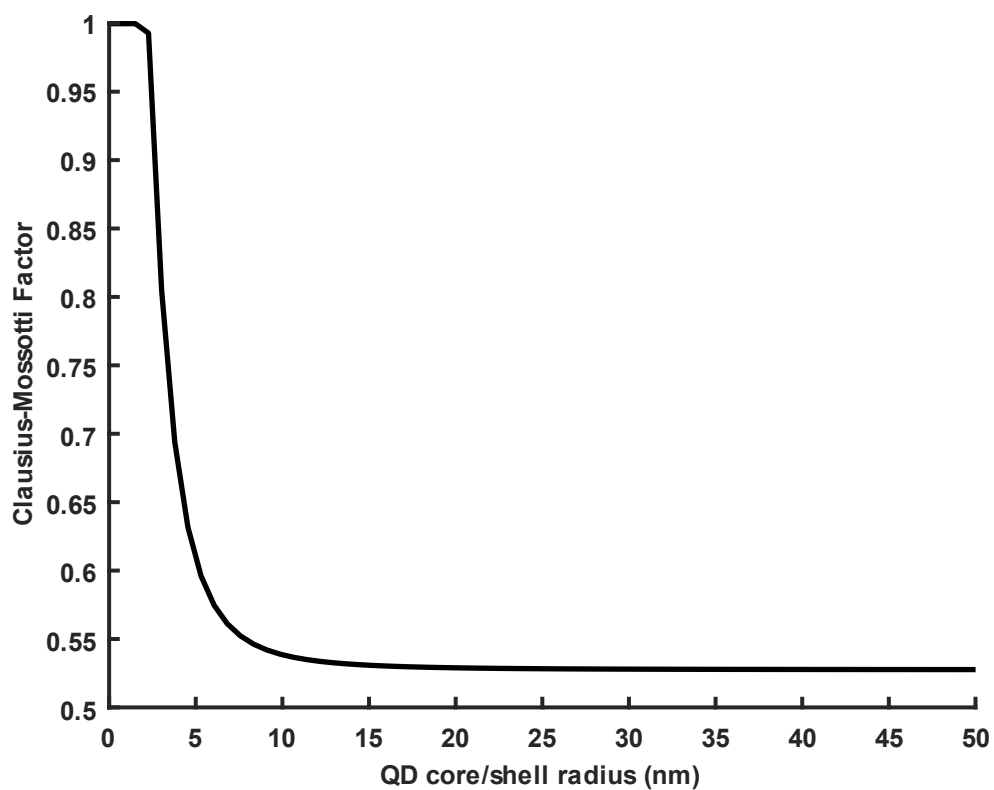
Supplementary Data 1



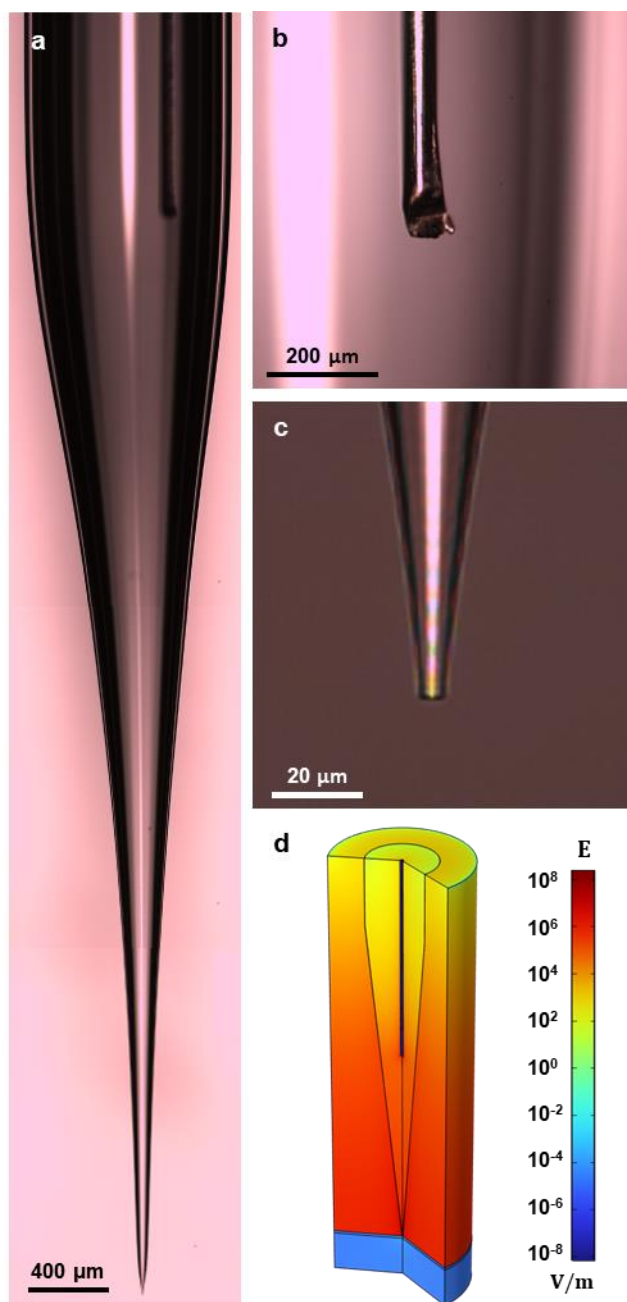
Supplementary Figure 1: COMSOL simulated particle geometries. Plotted gradient of the squared magnitude of the electric field, with respect to the vertical z-axis, of a faceted and spherical particle.



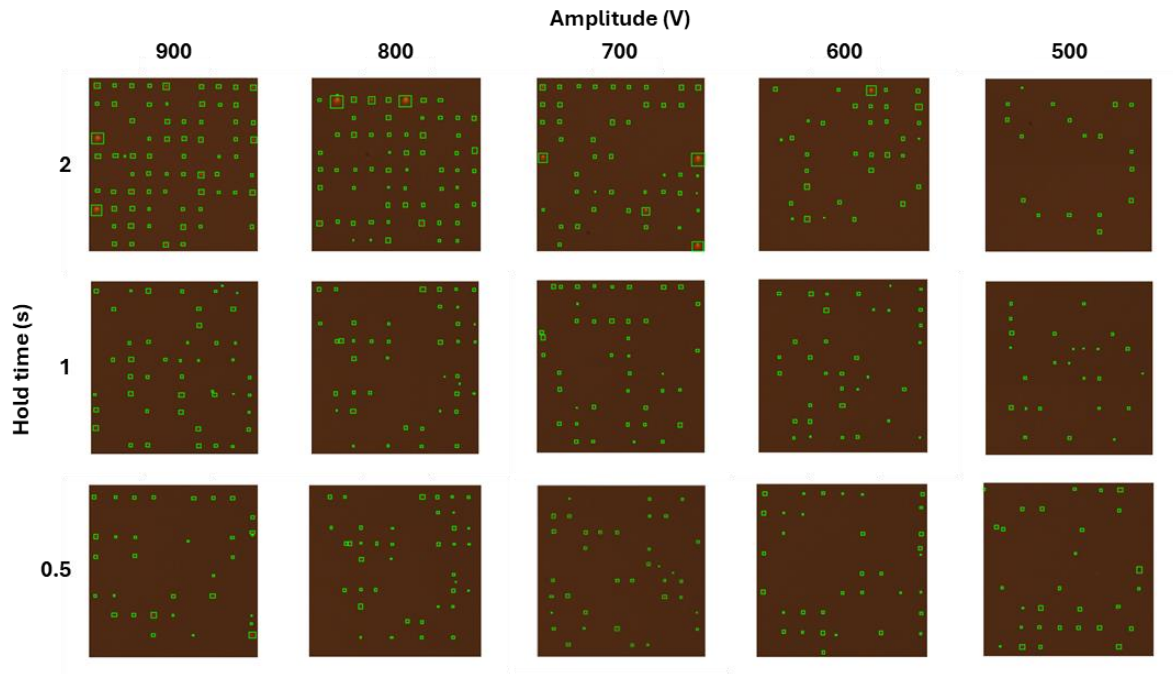
Supplementary Figure 2: Pendant drop test. Shadow image of octane:hexadecane pendant drop shape analysis. Pendant drop outline (blue) indicates shape profile used for surface tension measurement.



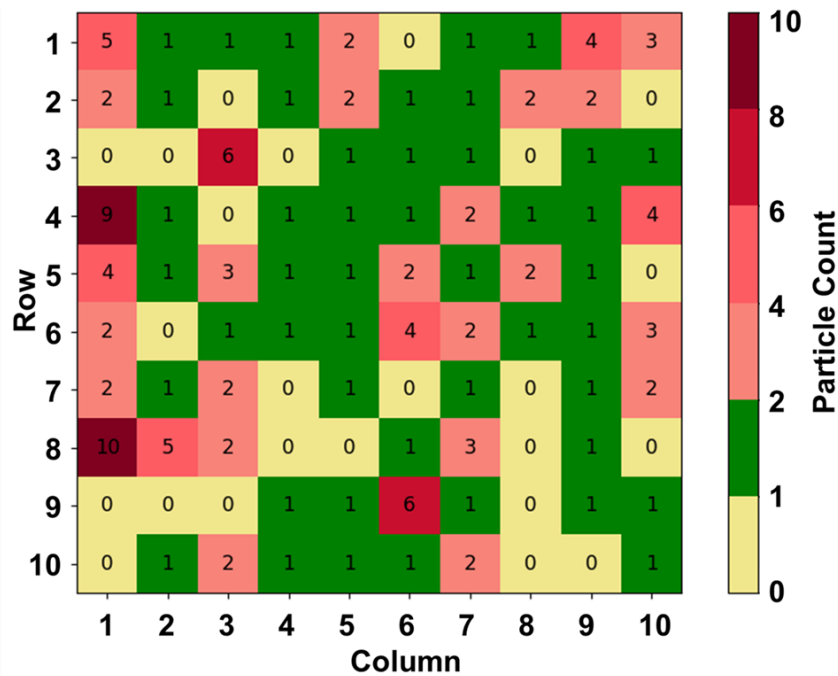
Supplementary Figure 3: Clausius-Mossotti factor for core/shell QD. Plotted approximation of Clausius-Mossotti factor of a core/shell QD based on the volumetric ratio between the CdSe core and CdS shell. The permittivity values (at 1 kHz) used for the CdSe core, CdS shell, and solvent medium used were: 20,000 (30), 8.7 (29), and 2.0 (30, 31), respectively.



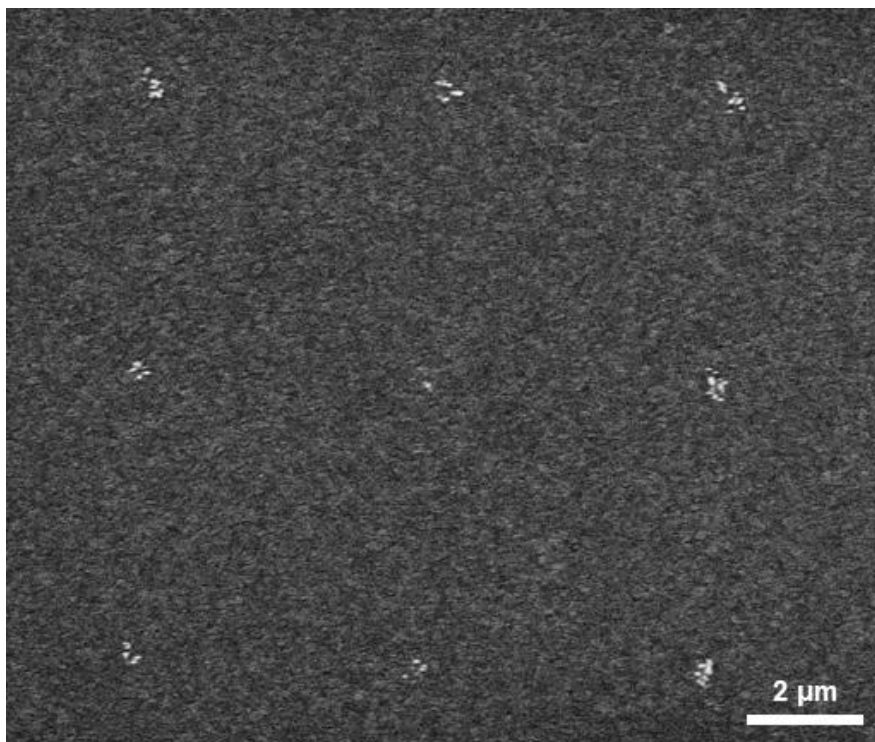
Supplementary Figure 4: Printhead analysis and simulation. a, b, and c, Brightfield microscopy images of (a) EHDIJ printhead, (b) interior electrode tip, and (c) printhead tip. (d) Finite element analysis simulating electric field in/around the printhead, substrate, and ground plane.



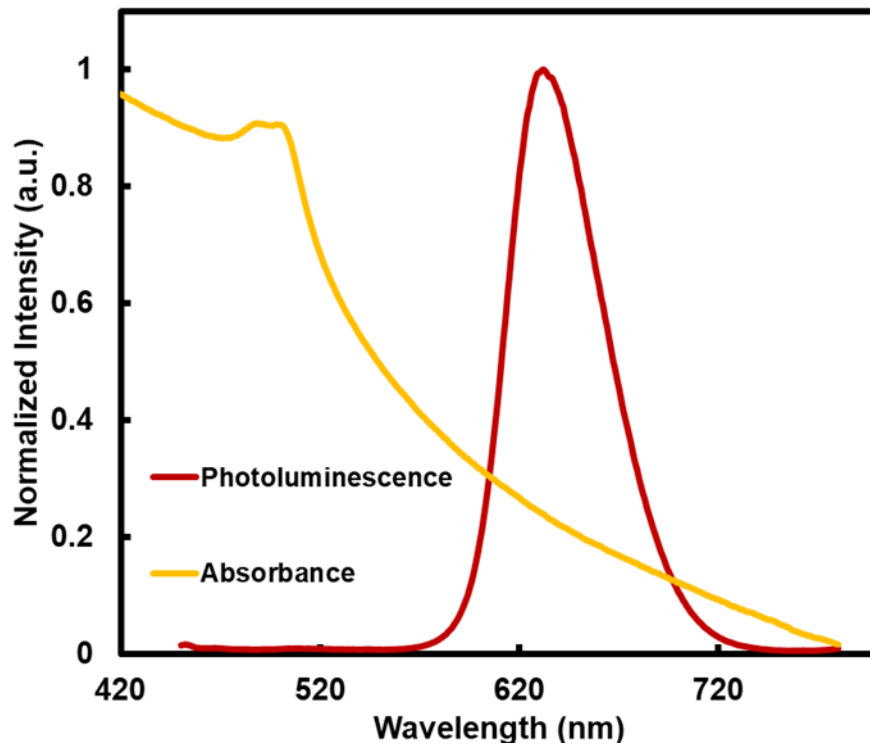
Supplementary Figure 5: MATLAB machine vision for print detection. Fluorescent microscopy images of EHDIJ prints in an array of amplitudes and hold times with 5 μm print spacing. Green boxes indicate discrete prints detected by MATLAB image processing toolbox.



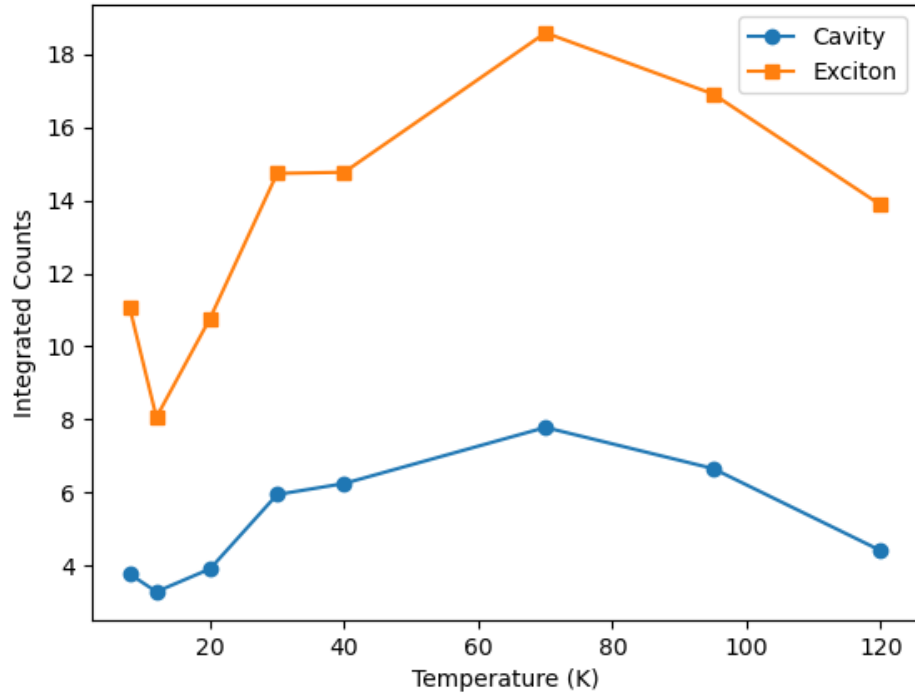
Supplementary Figure 6: Heatmap of SEM analysis. Plotted heatmap summary of the number of QDs counted per print attempt site, via SEM, for the 900 V and 2 s parameter configuration. Images from each print attempt site are included in Supplementary Data 1.



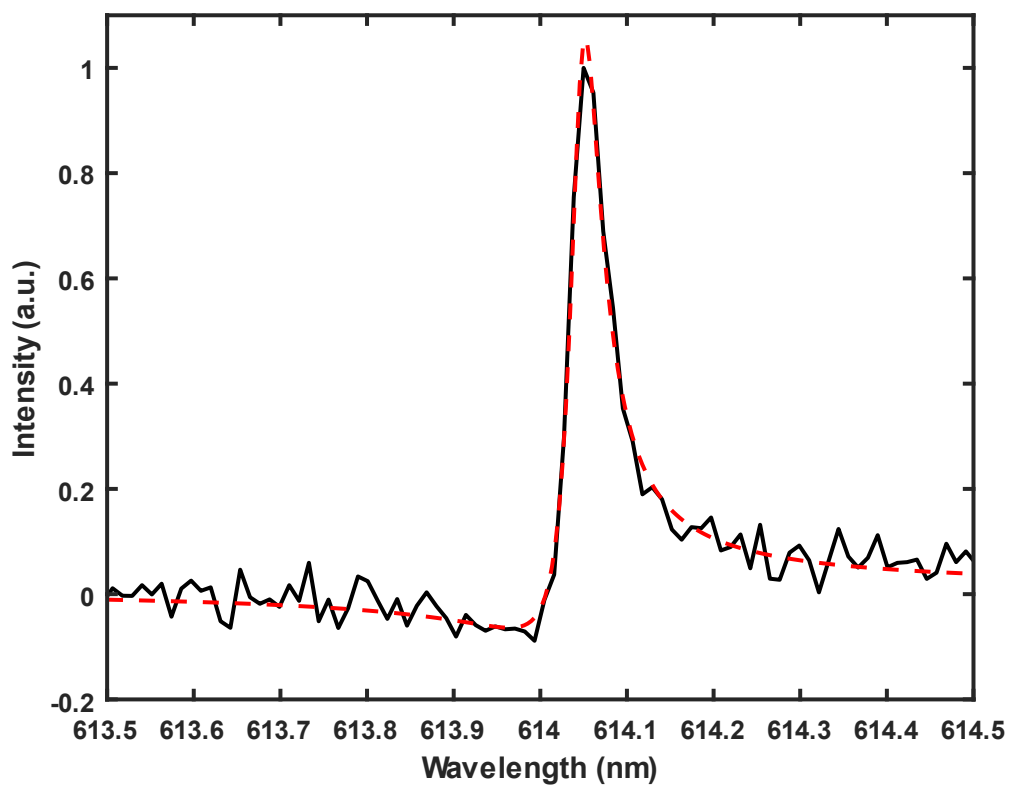
Supplementary Figure 7: Smaller colossal CdSe/CdS printing results. Scanning electron microscopy of 3x3 array of printed CdSe/CdS QD ensembles. Synthesized with 30 CdS monolayers, with an average diameter of 26.3 ± 2.2 nm.



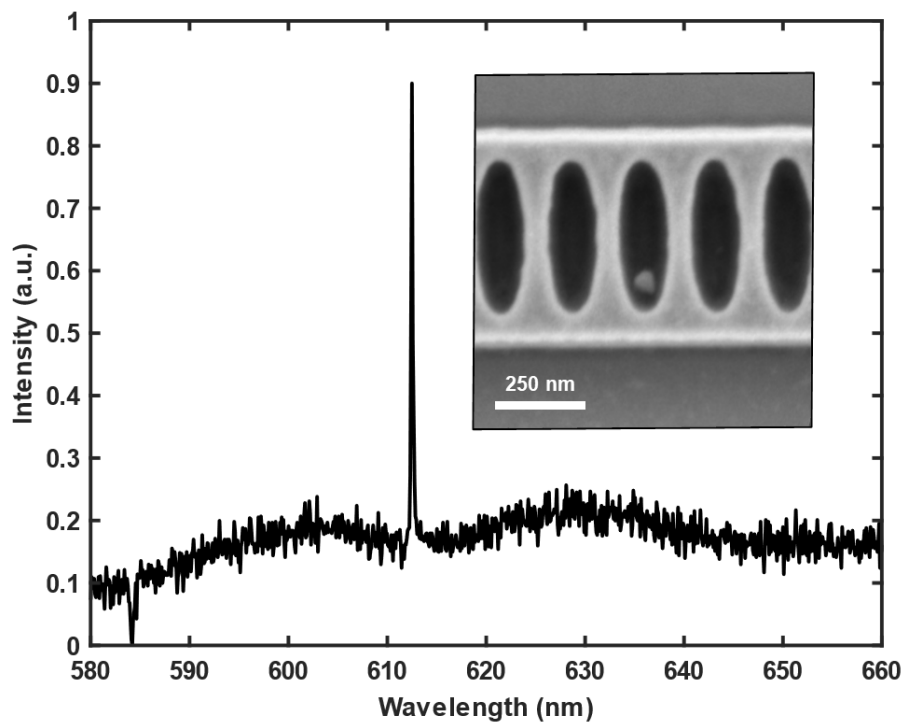
Supplementary Figure 8: Colloidal QD spectral characterization. Plotted spectrum of the Photoluminescence and absorbance of 80 ML CdSe/CdS QDs, as measured in hexane.



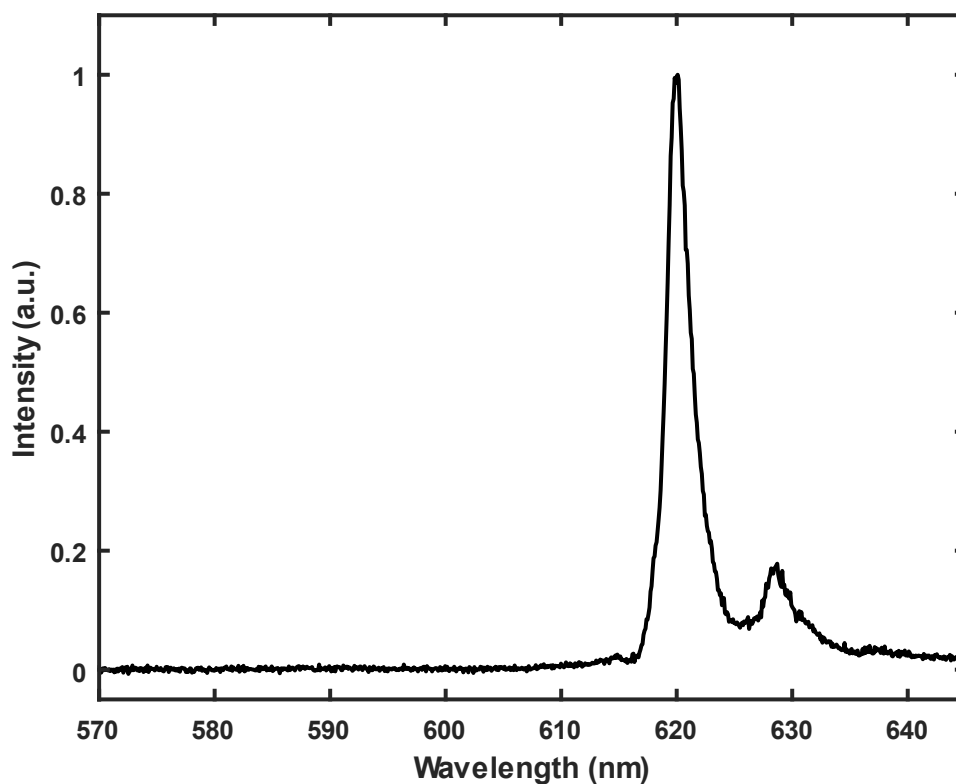
Supplementary Figure 9: QD-cavity temperature sweep. Plotted integrated counts of cavity mode and excitonic emission across a range of temperatures. Highest intensity of emission measured at 70 K.



Supplementary Figure 10: Spectrum of cavity mode. Plotted spectrum of QD-integrated cavity mode (black) with Fano fit (red). Measured at room temperature with 10 μW excitation.



Supplementary Figure 11: Photobleached heterointegrated QD-cavity. Plotted spectrum of heterointegrated QD that photobleached during spectral analysis, leaving only the SiN background and cavity mode emission. Inset: SEM image of EHD-printed QD in cavity.

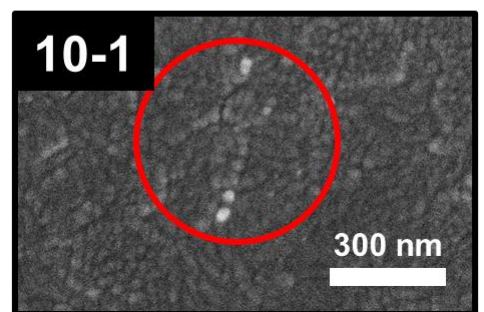
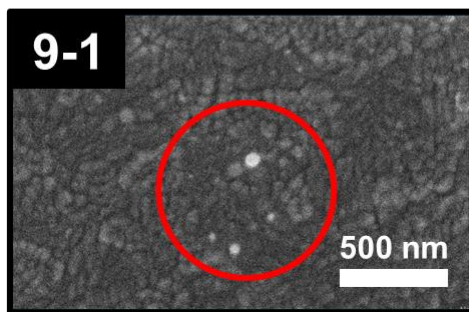
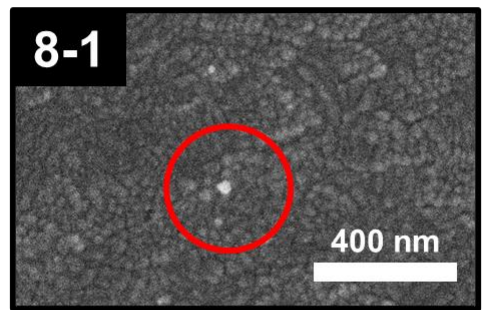
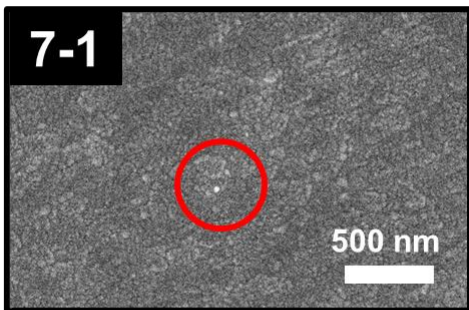
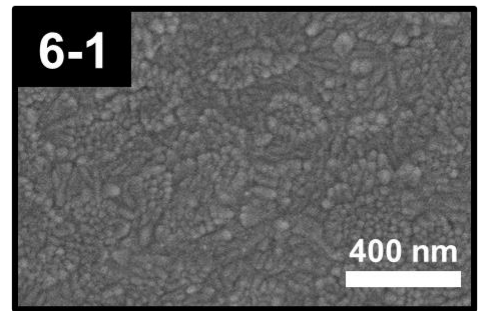
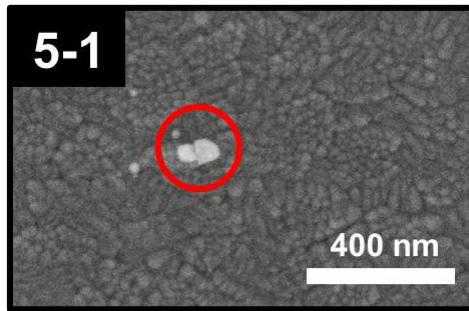
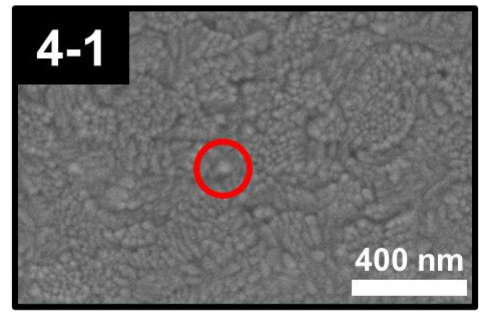
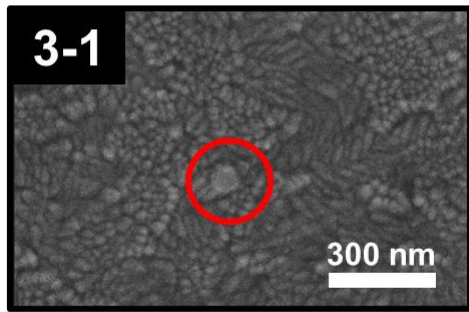
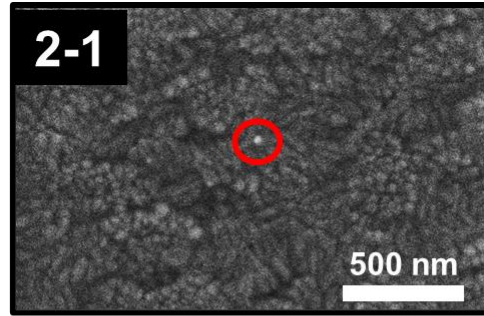
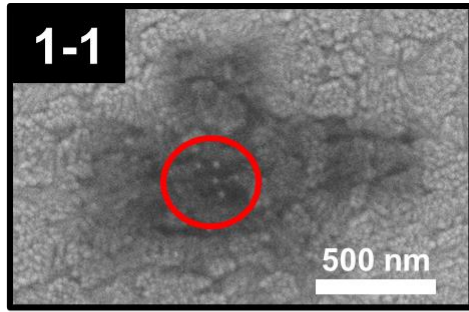


Supplementary Figure 12: Spectrum of colossal CdSe/CdS QD at 8 K. Plotted spectrum of colossal CdSe/CdS QD (80 CdS monolayers) measured at 8 K and 1 μ W excitation. Measured on SiO₂ substrate.

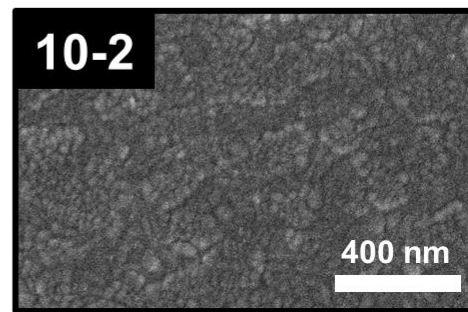
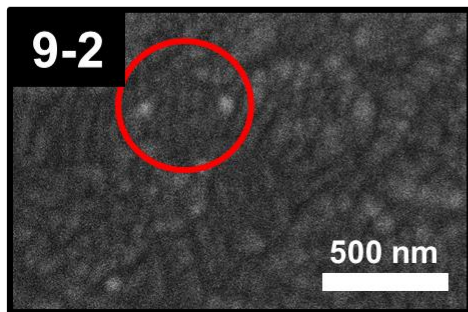
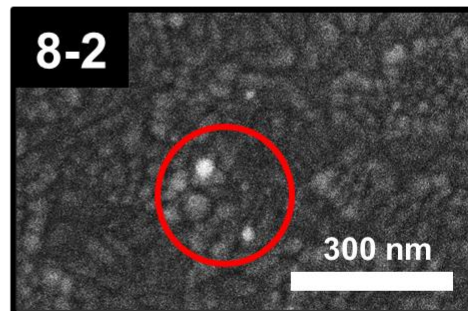
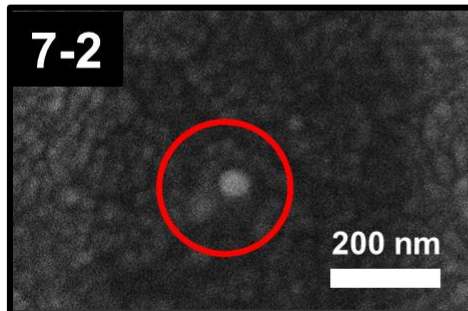
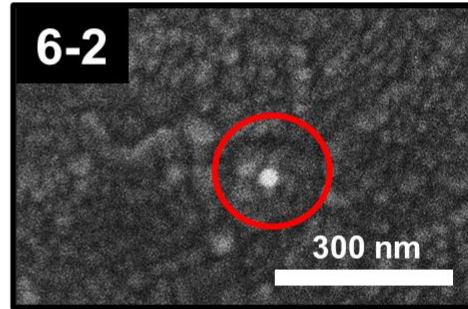
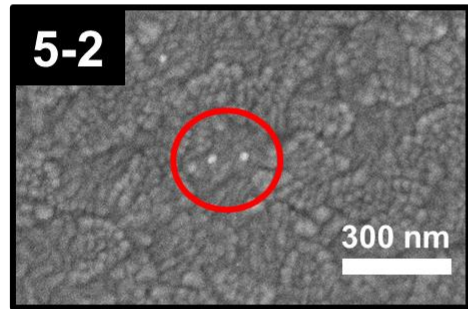
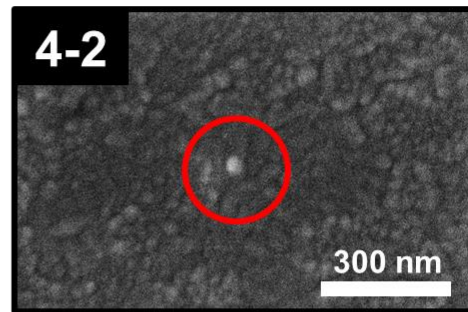
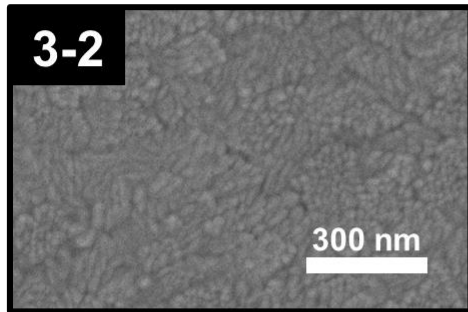
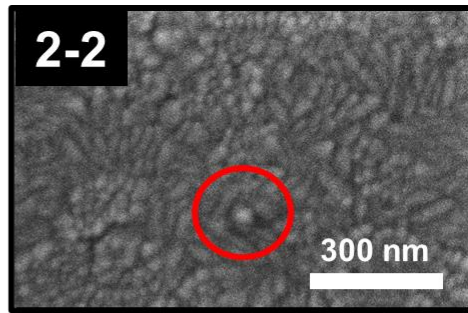
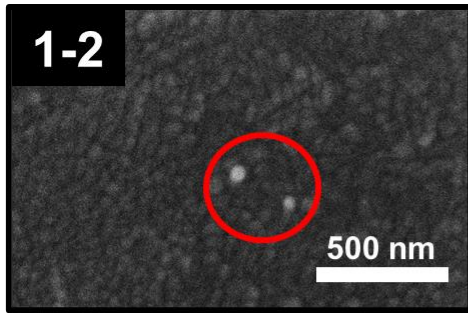
Supplementary Data 1 (separate file)

A tabulated micrograph summary of the SEM analysis of the 900 volt and 2 second printing parameter configuration. Data includes SEM images of each print attempt site, with indicators for the position of the found QD(s).

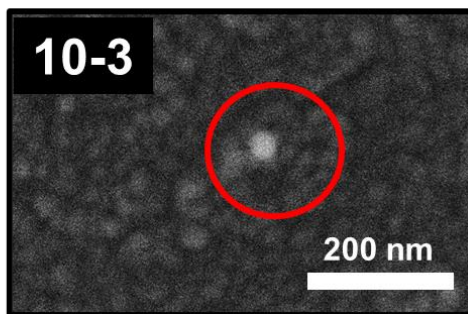
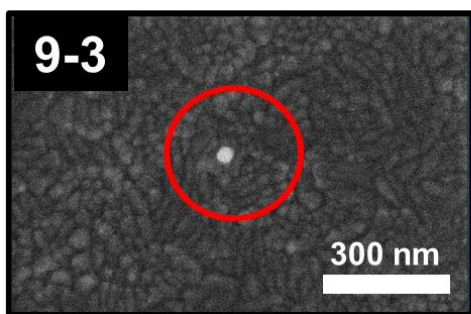
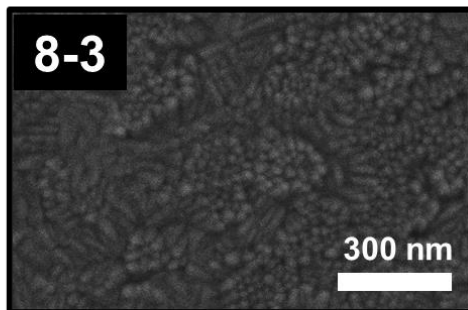
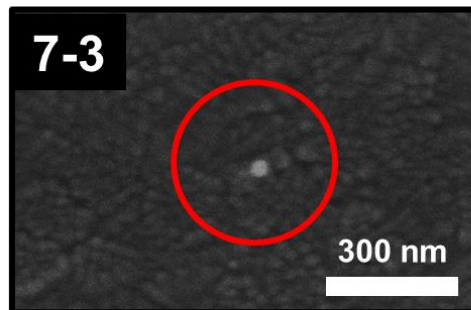
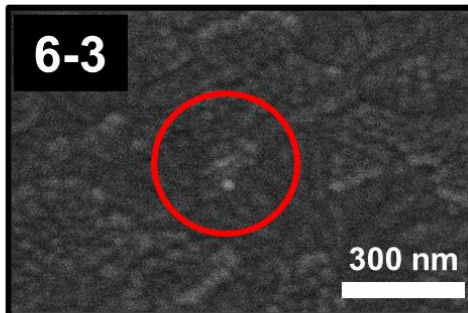
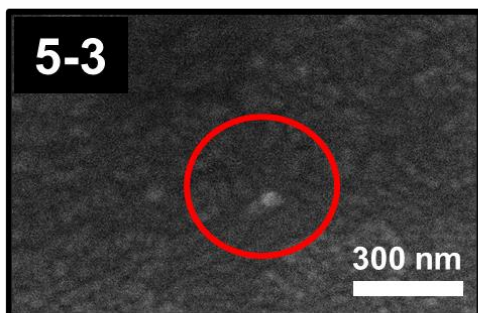
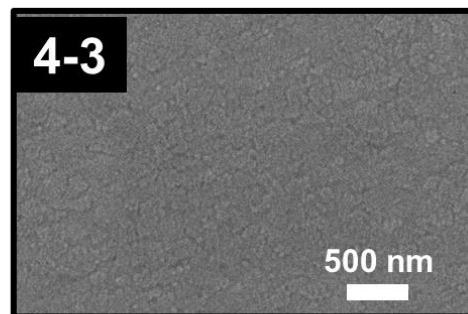
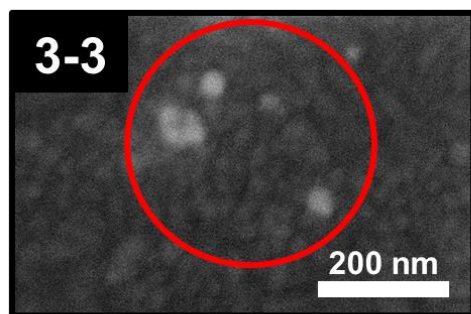
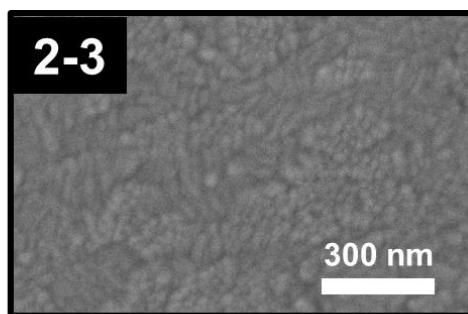
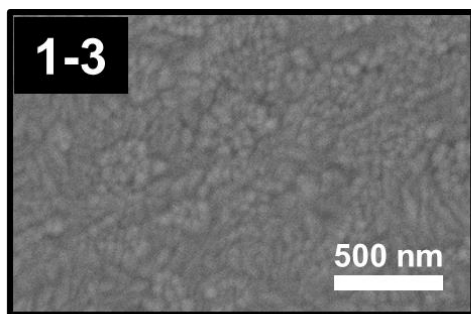
Row 1



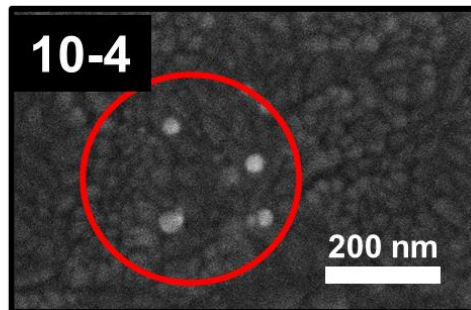
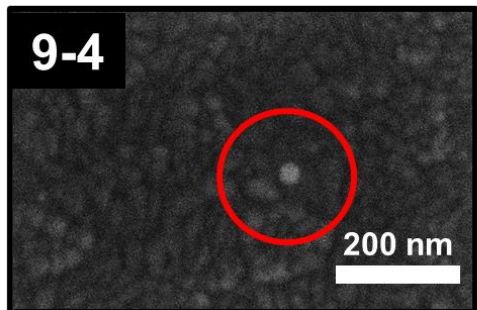
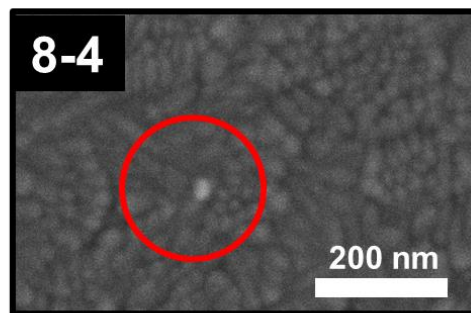
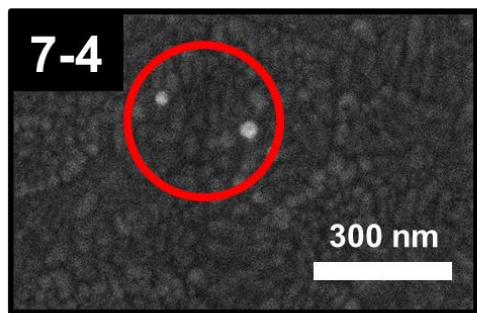
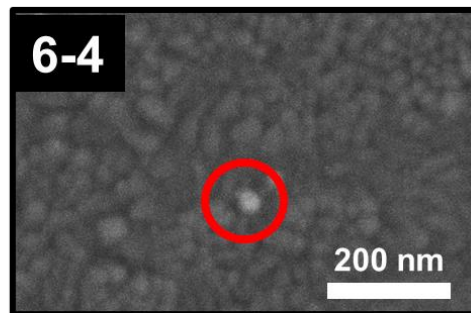
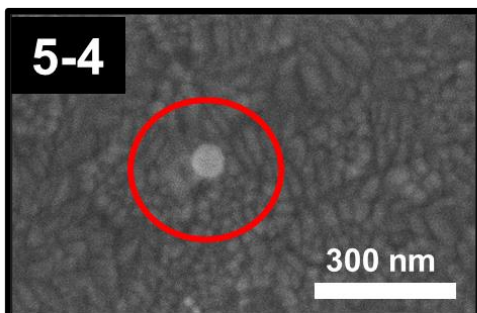
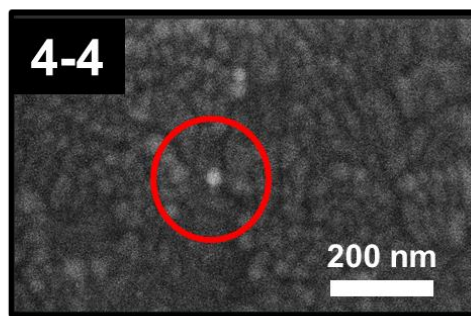
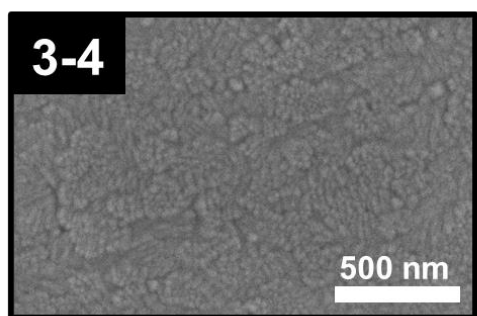
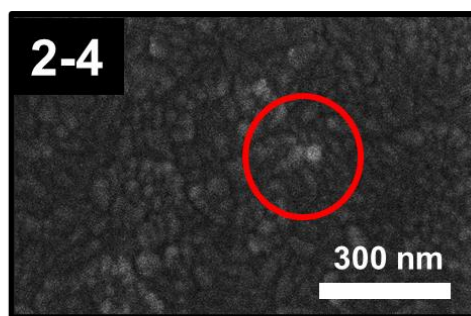
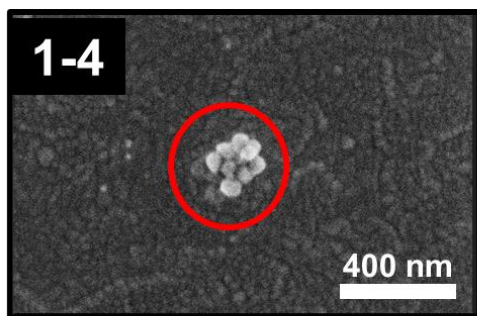
Row 2



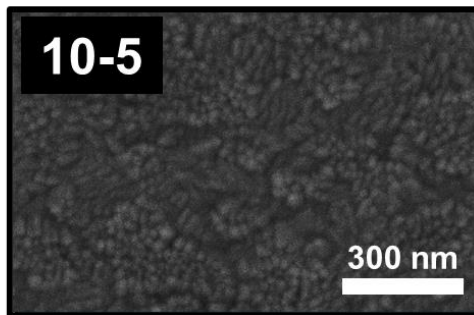
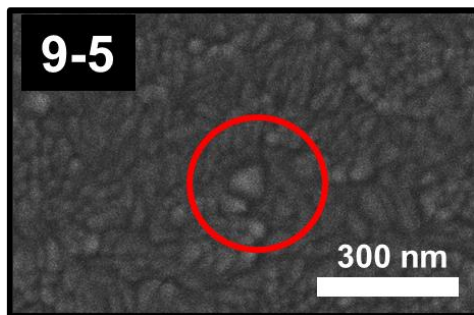
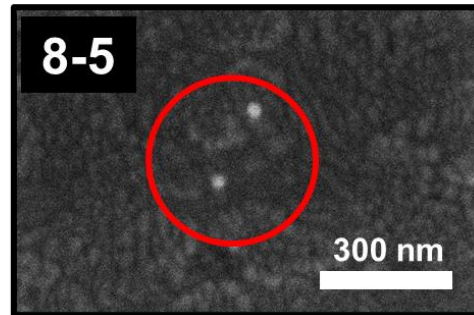
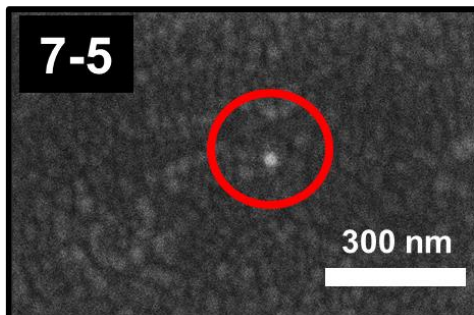
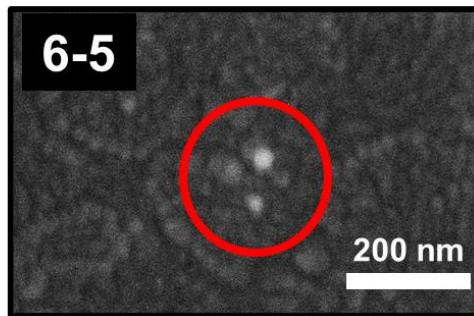
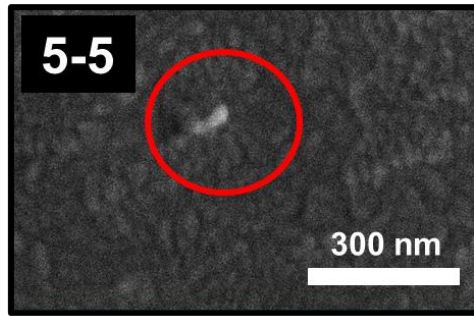
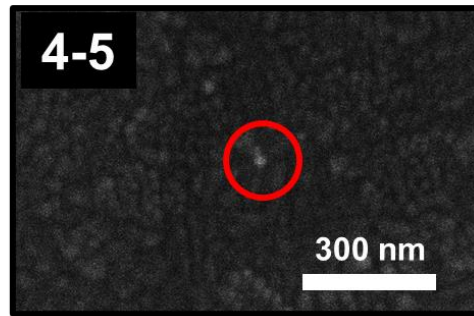
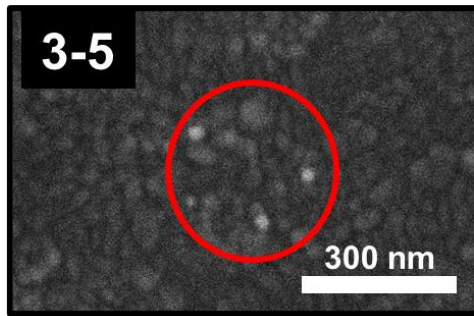
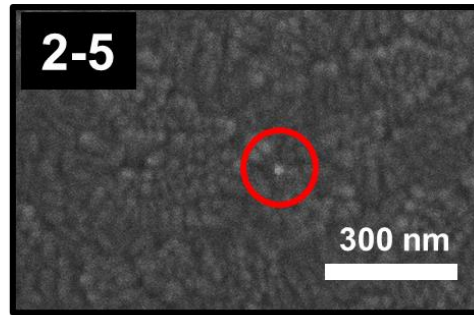
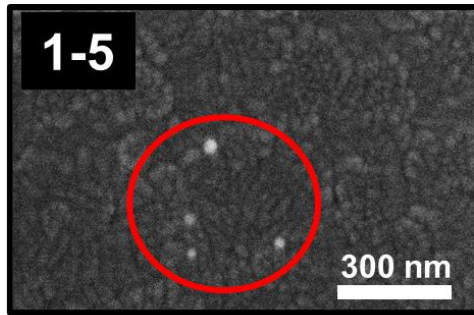
Row 3



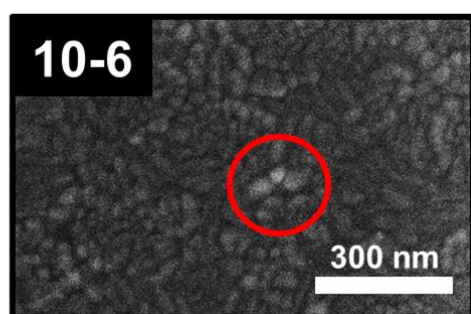
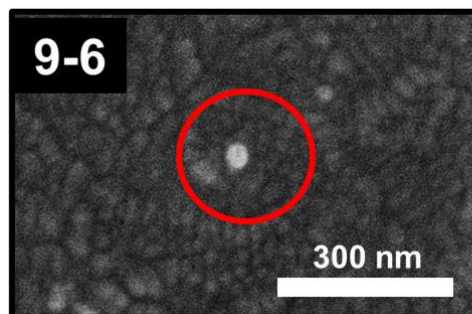
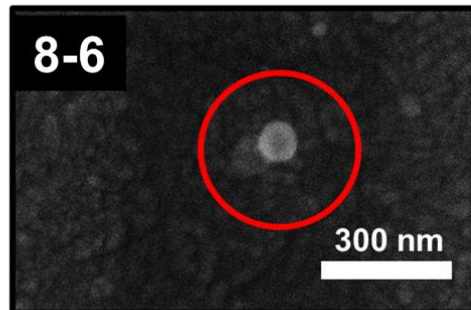
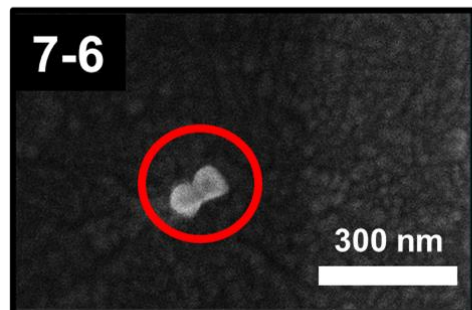
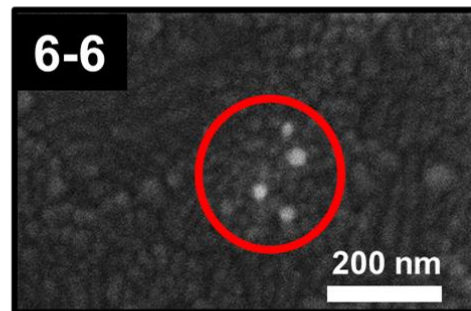
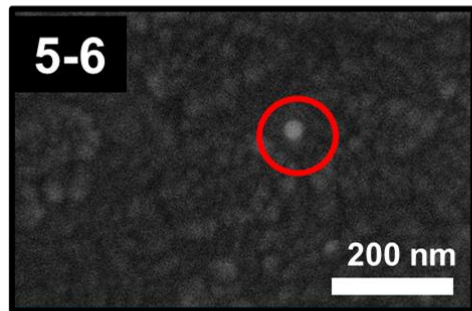
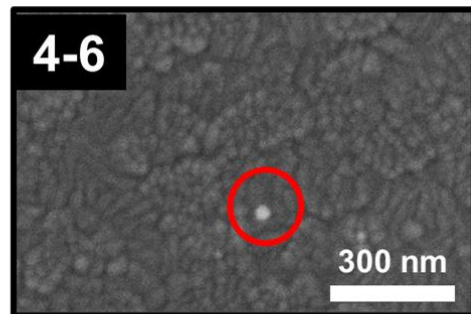
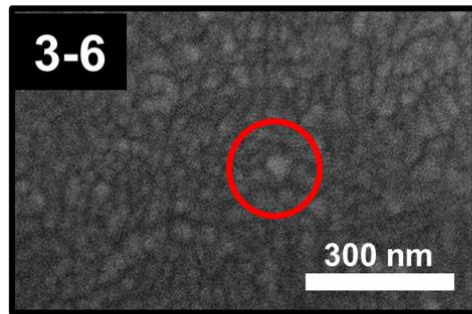
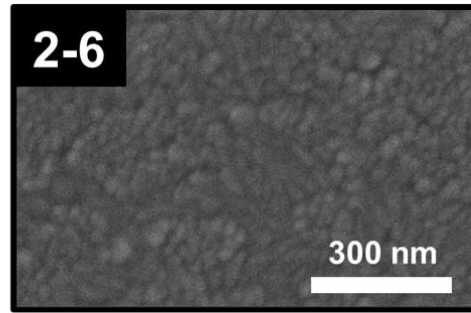
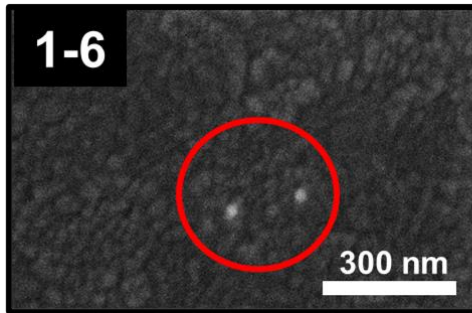
Row 4



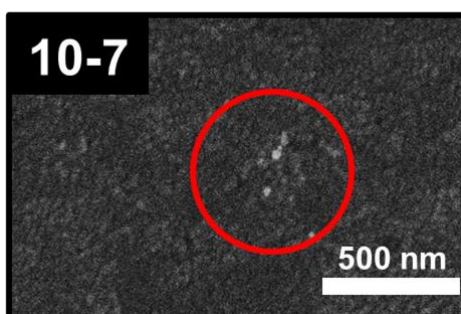
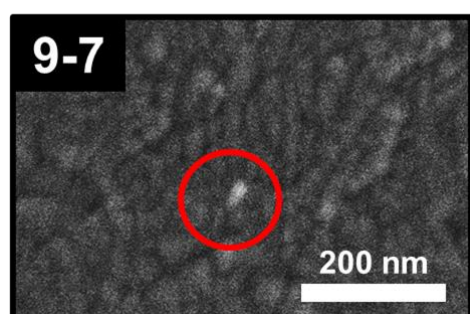
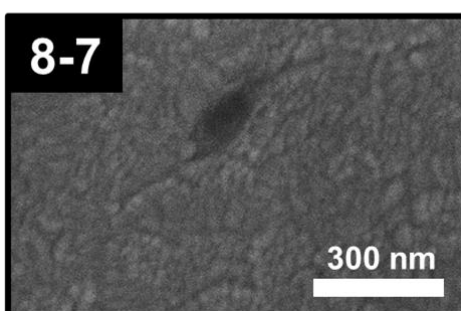
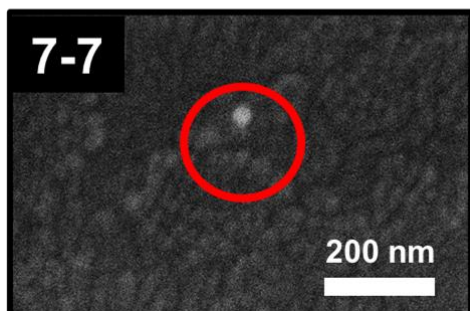
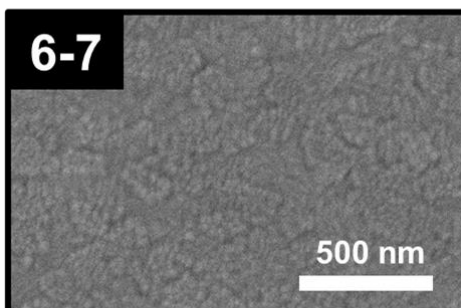
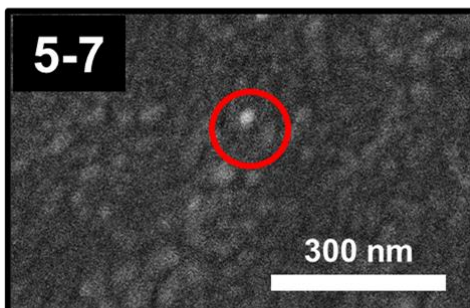
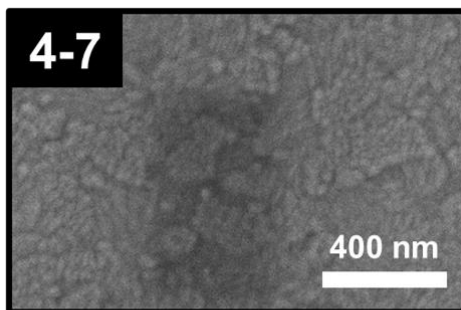
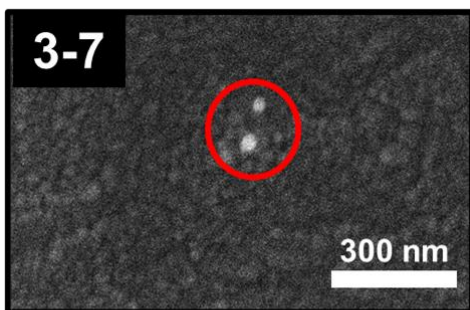
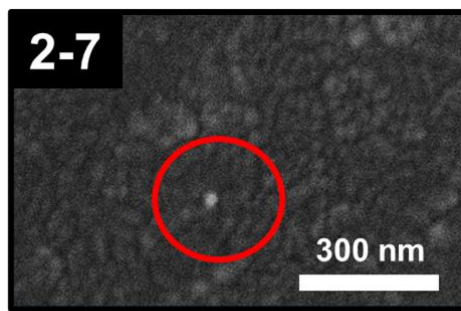
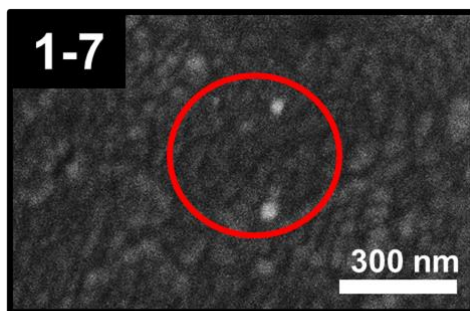
Row 5



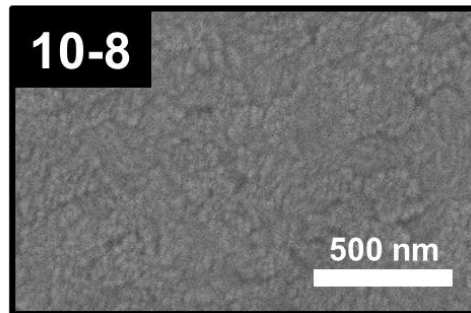
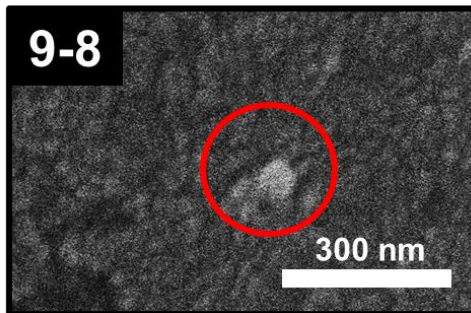
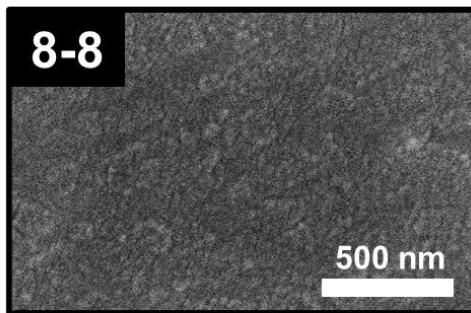
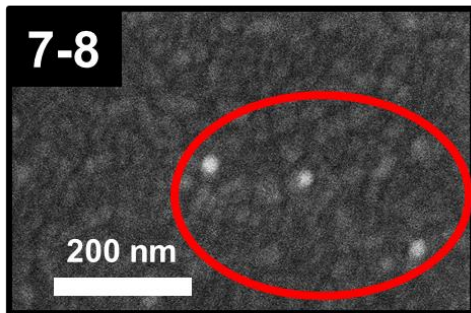
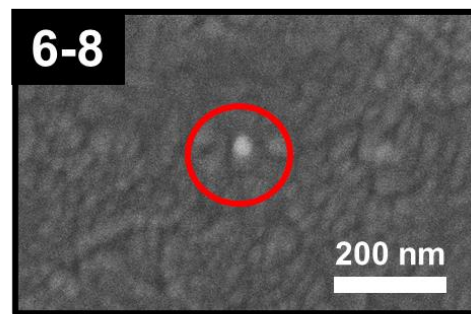
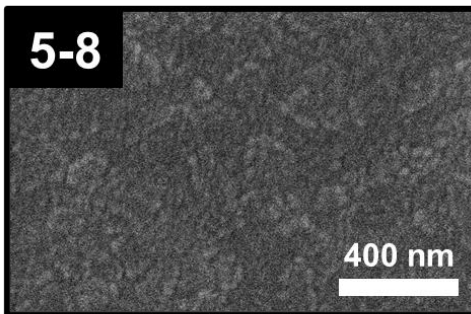
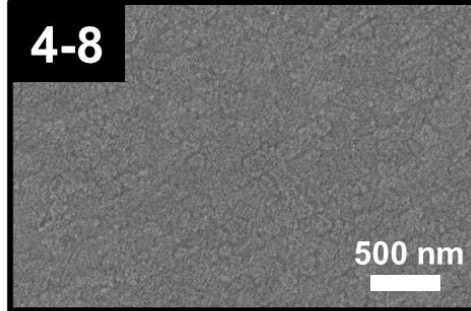
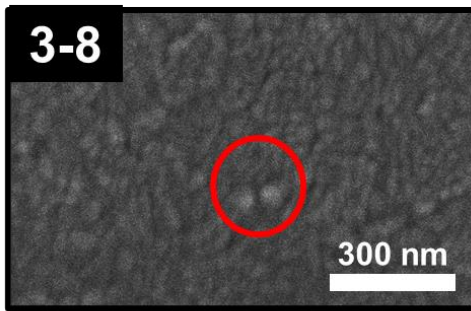
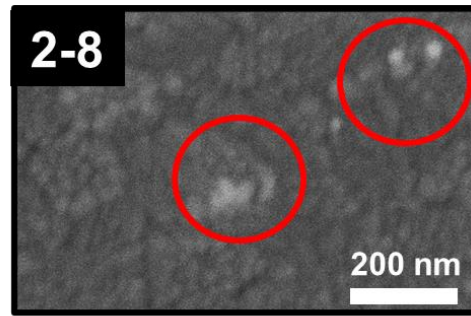
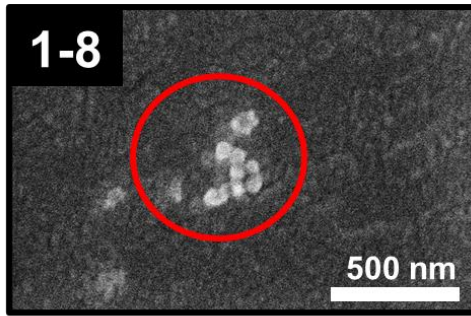
Row 6



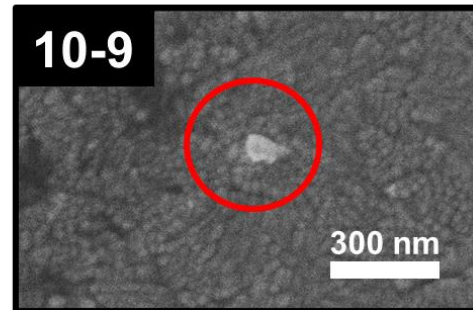
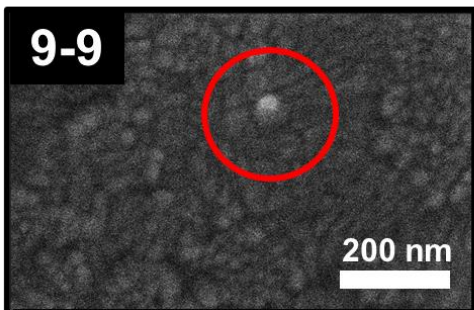
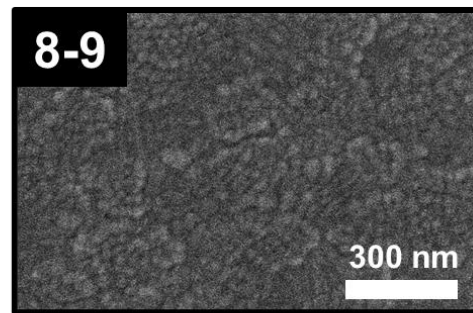
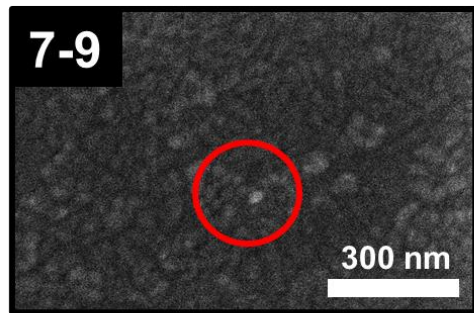
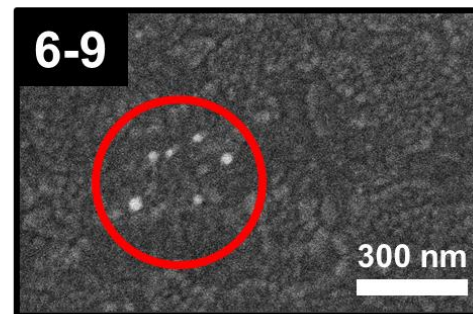
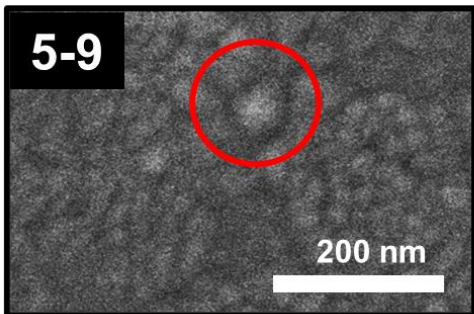
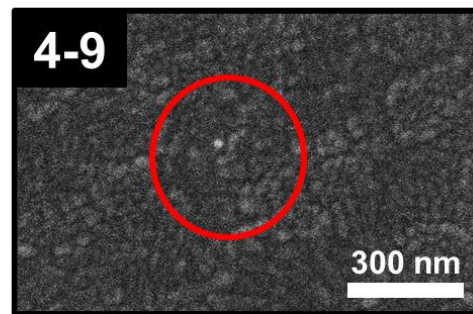
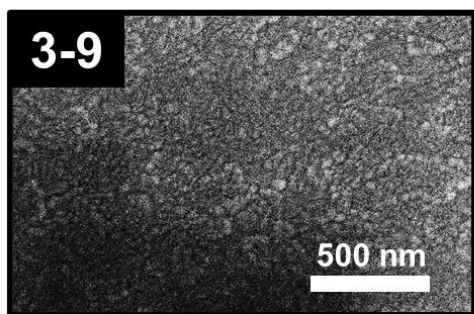
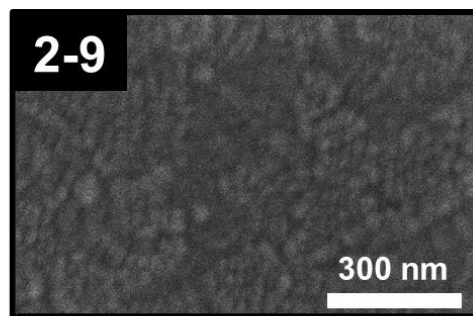
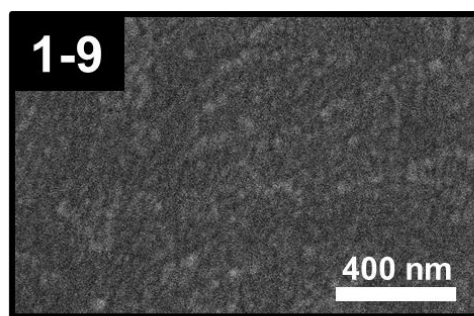
Row 7



Row 8



Row 9



Row 10

